



Electrode-Level Modeling of Silicon Anodes for Improved Cell Design

Amir-Sina Hamed¹, Edmund M. Shumway, and Dean R. Wheeler²

Department of Chemical Engineering, Brigham Young University, Provo, Utah, United States of America

Silicon has a remarkably high specific capacity as a Li-ion battery anode material; however, its large volume expansion and contraction make it extremely challenging to use. This work introduces a pseudo-2D (P2D or Newman-type) model that incorporates the distinctive mechanical and electrochemical behaviors of porous electrodes with large volume changes characteristic of silicon and similar active materials. Localized volume change is propagated rigorously to other electrode variables, considering elastic, plastic, and chemical strains; associated advection and hysteresis; the presence of a fluid reservoir and packaging adjacent to the cell stack; nonlinear electrode swelling behavior; deactivation of active material; and the effect of stress on open circuit potential. A silicon half-cell model is carefully parameterized by previously published experiments, and indeed provides insights in how to interpret the experiments and shows where some are problematic. The model is used as a digital twin to predict the degree of electrode utilization for different packaging designs and active material loadings, thereby allowing improved cell design.

© 2024 The Author(s). Published on behalf of The Electrochemical Society by IOP Publishing Limited. This is an open access article distributed under the terms of the Creative Commons Attribution Non-Commercial No Derivatives 4.0 License (CC BY-NC-ND, <https://creativecommons.org/licenses/by-nc-nd/4.0/>), which permits non-commercial reuse, distribution, and reproduction in any medium, provided the original work is not changed in any way and is properly cited. For permission for commercial reuse, please email: permissions@iopublishing.org. [DOI: [10.1149/1945-7111/ad9fe4](https://doi.org/10.1149/1945-7111/ad9fe4)]



Manuscript submitted October 20, 2024; revised manuscript received December 11, 2024. Published December 30, 2024.

Nomenclature

α	Charge-transfer coeff, anodic	D_e	Diffusivity, electrolyte
β	OCP hysteresis speed parameter	E	Elastic modulus, porous film
γ	Bruggeman coeff, electrolyte	E_a	Elastic modulus, active matl
ϵ	Volume fraction, pores	E_n	Elastic modulus, inert solids
ϵ_a	Volume fraction, active matl	E_s	Elastic modulus, solid phase
ϵ_n	Volume fraction, inert solids	$\mathcal{E}_{\text{cell}}$	Cell electric potential
ζ	OCP hysteresis switching functn	f_{\pm}	Mean ionic activity coeff
η	Surface overpotential	\mathcal{F}	Faraday's constant
θ_*	Chemical strain	F_{res}	Reservoir lateral flow
θ_p	Plastic strain	F_Y	Yield function (* strain version)
θ_x	Total strain, x direction	g	Film swelling coefficient
θ_y	Total strain, y direction	h	Secondary swelling coefficient
θ_D	Deviatoric strain	i_0	Exchange current density
θ_V	Volumetric strain	i_0^{ef}	Exch curr density at ref conc
θ_Y	Yield strain, harmonic mean	I_{app}	Current dens, externally applied
κ_e	Ionic conductivity, electrolyte	I_e	Current dens, electrolyte phase
κ_s	Electronic conductivity, solid	I_s	Current density, solid phase
μ_i	Species electrochemical potential	J_a^{rxn}	Li molar flux, reaction surface
ν	Poisson's ratio, porous film	J_a	Diffusive Li radial flux, active
ν_s	Poisson's ratio, solid phase	J_e	Diffus Li planar flux, electrolyte
ρ_0	Dry electrode initial density	k	Poisson's ratio combination
ρ_i	Species skeletal density	L	Layer thickness
ρ_s	Combined solid skeletal density	L_θ	Local-strain-corrected thickness
σ_x	Cell-sandwich normal stress	m, ℓ	Mix-rule microstruct exponent
σ_y	Tangential stress	M	Modulus, constrained film
σ_Y	Yield strength, harmonic mean	\mathcal{M}_i	Species molecular mass
τ_p	Time constant for plastic strain	N_a	Total Li radial flux, active
ϕ_{a0}	Solid vol frac, functnl active matl	N_e	Total Li planar flux, electrolyte
Φ_e	Electric potential, electrolyte	\mathcal{N}_M	MacMullin number, electrolyte
Φ_s	Electric potential, solid phase	P°	Pressure, 1 bar standard state
χ_a	Fractional capacity, active matl	P_a	Surface pressure, active material
a_a	Ratio, active area to electrode vol	q_a	Running capacity per active mass
b_Y	Yield asymmetry parameter	Q_a	Electrode areal charge capacity
C_a	Li concentration, active matl	r	Particle radial coordinate
C_a^H	Host concentration, $=V_a^{-1}$	\mathcal{R}	Universal gas constant
C_a^*	Li conc, active, dimensionless	R_a	Radius, active particle
C_e	Li concentration, electrolyte	s	State of lithiation (SoL)
D_a	Diffusivity, active matl	t	Time
		t_+^0	Cation transference number
		T	Absolute temperature
		U	Open-circuit potential (OCP)
		U°	OCP at standard state 1 bar
		U_\pm°	OCP for lithiation/delithiation

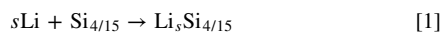
²E-mail: dean_wheeler@byu.edu

v_r	Velocity, r direction
v_x	Velocity, x direction
V	Molar volume, porous film
V_a	Molar volume, active matl
V_s	Molar vol, active plus inert solids
\bar{V}_i	Species partial molar volume
w_i	Species dry mass fraction
x	Cell normal coordinate
y	Cell tangential coordinate

Beginning with the seminal paper by Doyle, Fuller, and Newman,¹ pseudo-2D (P2D or Newman-type) models have proven their value over the last 31 years due to their well-devised combination of computational efficiency and physical fidelity, enabling improved design, optimization, and control of batteries. The original model and subsequent variants incorporate key drivers of cell behavior while avoiding expensive accounting of individual particles and pores by homogenizing the 3D microstructure.^{2,3} The goal of this work is to develop and present a P2D model that accurately describes the distinctive mechanical and electrochemical behaviors of a cell containing distributed active material that undergoes large and localized volume changes. The model is used as a digital twin for predicting and understanding *in silico* the performance of silicon-based Li-ion cell designs.

Challenges with the use of silicon active material

Due to its exceptional theoretical specific capacity and low operating potential, silicon is the leading candidate for alloy-type negative electrode active materials. Lithiation of silicon proceeds via a simple addition-type reaction that can be expressed as



where s is the state of lithiation (SoL) and reaches a maximum of 1 for room-temperature cycling. This corresponds to a capacity of 3578 mAh/g Si and a particle volume change of 275%.^{4,5} For comparison, the common intercalation-type electrode materials graphite and LiCoO₂ undergo 13% and 2% respective volume changes upon full lithiation.

The key problem with the use of silicon and similar alloy-type active materials is capacity retention in cycling. Capacity loss upon lithiation and delithiation may be due to continued solid-electrolyte interphase (SEI) formation, Li trapping in the host alloy, loss of particle electrochemical contact, or other mechanical effects when particles undergo large volume changes.^{4,6} A commonly proposed remedy for Si is to form nanoscale (≈ 50 nm) particles, rods, or thin films to ameliorate stress-induced cracking.^{7,8} Improved polymeric binders have also been sought. For instance, sodium carboxymethyl cellulose (CMC) and variants were identified as potential improvements over conventional polyvinylidene fluoride (PVDF) binder.⁹ Another accepted commercial strategy is to combine graphite with silicon in electrodes to moderate the expansion and contraction to an acceptable level while taking advantage of silicon's higher capacity.

Given the above issues, for a more reliable Si-based cell design we must understand quantitatively how volume changes of active material affect electrode behavior. Moreover, localized volume changes are expected to occur in silicon anodes under high-rate charge and discharge when the SoL becomes nonuniform across the electrode. Given the difficulty in experimentally determining such localized effects, a suitable mathematical model can give needed insight. As context for our proposed P2D model, we now briefly survey previous modeling efforts for Si-based electrodes.

Challenges in P2D modeling of silicon electrodes.—A considerable number of mathematical models have been developed to better understand pure Si/SiO_x or blended Si-C anodes. While it is tempting to ignore the volume change of Si particles and treat them as traditional P2D models have treated graphite or cathode particles,^{10,11} we judge this as not sufficiently realistic. Instead, particle size, film porosity, and

film thickness must become dynamic variables; ramifications on all other cell properties must also be considered.

The P2D model gains computational efficiency by homogenizing the 3D structure and order reduction of the governing equations. Multiple single-particle or 3D studies have focused on the mechanical aspects of Si particle growth and subsequent effects on the electrode.^{12–19} It can be difficult to integrate such models with a P2D model, considering issues of computational cost, order reduction, homogenization, and the need to parameterize unknown material parameters. For instance, the work here requires careful parameterization of composite material properties such as diffusivity, elastic modulus, and yield strength that can be highly sensitive to electrode composition, state of lithiation, and porosity.

Two early studies by Chandrasekaran and Fuller considered Si particle volume change along with variations in solid diffusion and porosity of the anode.^{20,21} They did not include the effects of stress and strain and the associated volume change of different cell sandwich layers. Later studies have utilized a similar approach to simulate the capacity loss of Si anodes during cycling.^{22,23}

In modeling Si electrodes, one must appropriately treat lithiation-induced changes to film layer thickness and porosity while further considering possible confinement from the cell packaging. The Weidner group published a series of papers modeling volume changes in porous electrodes, especially silicon electrodes.^{24–29} They introduced an important experimentally determined parameter called the swelling coefficient. The material conservation equation uses this parameter to estimate how much volume change occurs within the electrode. These works present a reasonable balance in detail between the electrochemical and mechanical aspects of Si electrodes and capture many important physical artifacts within Si electrodes. Nevertheless, we propose some improvements to the strain and conservation expressions and to generalize the swelling coefficient in order to match available electrode dilatometry data and to incorporate limits on the packing fraction of solids.³⁰

The Wu group recently developed an electrochemical-thermal-mechanical model that deals with stress distribution in silicon-graphite anodes.^{31,32} The model accounts for swelling due to thermal strain, in addition to lithiation and stress-induced strains. The model also can track local particle-cracking behavior that results from stress gradients. However, strain in the composite electrode is treated in a spatially averaged, not local, sense. Other multiscale models likewise use electrode-average lithium concentration to find electrode-average strain, as opposed to finding local strain from local lithium concentration.^{16,17} As mentioned above, such simplification restricts model accuracy to low rates of charge or discharge.

Arisetty et al.³³ developed a model of Si electrodes that importantly considers local changes in porosity, cell thickness, and resistance. However, their development lacks a closure relationship (e.g., swelling coefficient) that determines how Si expansion contributes to film thickness vs. porosity, meaning the model is under-specified by one degree of freedom.

Lastly, in attempting to formulate a physically accurate Si-based porous electrode model, we should consider four additional phenomena that accompany large volume changes but that are almost universally neglected in prior work: (1) The expansion and contraction of active particles readily produce plastic yielding at the electrode level. To wit, significantly re-sized active particles must necessarily rearrange their packing structure because the current collector does not experience a commensurate dimensional change. Thus, we must include plastic and not just elastic mechanics in the electrode model. (2) Expansion and translation of particles lead to substantial decay from the theoretical capacity. Thus, the model must appropriately deal with “dead” active material that continues to occupy volume, in addition to the typically large volume fraction occupied by the carbon-binder domain. (3) Particle and pore volume changes lead to the advective motion of lithium. Both electrolyte and solid-phase lithium mass conservation equations must properly account for this advective motion. Relatedly an electrolyte reservoir lateral to the 1D cell sandwich is needed and cannot be assumed away (cf.²¹). (4) Electrode swelling can lead to large normal and

tangential electrode stresses, which in turn can have a substantial effect on open circuit potential.

The model developed in this study can be implemented as a relatively low-cost extension to a conventional P2D model. The model description is quite lengthy, however, because it requires adding to and generalizing the core equations of P2D models developed over the last 31 years.

Model Development

First principles are used to incorporate mechanical aspects into a traditional P2D cell model. Specifically, we determine how volume changes in active particles dynamically propagate to mechanical and then electrochemical variables. Along the way, we determine needed mechanical properties from published experiments.

Volume of active particles.—The principal driving force for mechanical change in the electrode is chemical strain of the active particles. It is well understood that a temperature change in a material can cause a volume change. Comparatively, lithiation in active materials can lead to a much larger and localized volume change, especially in the case of silicon.

Our particle-level mechanical model is relatively simple. For individual active material particles, we assume an isotropic material that is relatively rigid. This means that elastic strain due to stress external to the particle is small in magnitude compared to chemical strain. Similarly, while plastic strain inside the particle relaxes residual stresses, it does not substantially affect the overall particle volume and is neglected in the present model, except for the hysteresis we include in the open circuit potential (OCP, see Eq. 61).

The relationship between the SoL and volume of amorphous Li-Si alloy is shown in Fig. 1. It is common in Si modeling studies to treat the alloy as a chemically ideal mixture or equivalently to make constant the partial molar volumes of solute and host. The Fig. shows that this is not accurate at low degrees of lithiation as indicated by the change in slope. The piecewise fitted curve is

$$\frac{V_a}{V_{a0}} = 1 + \begin{cases} \frac{539}{96}s^2, & s < \frac{2}{7} \\ \frac{77}{24}s - \frac{11}{24}, & s \geq \frac{2}{7} \end{cases} \quad [2]$$

where fractions are used in the coefficients to allow arbitrary numerical accuracy in a subsequent inversion procedure. V_a indicates volume per mole of host, defined as species $\text{Si}_{4/15}$ in Eq. 1. $V_{a0} = \frac{4}{15}\mathcal{M}_{\text{Si}}/\rho_{\text{Si}} = 3.2157 \text{ cm}^3/\text{mol}$ for the pristine active material. Subscript 0 throughout this work indicates an initial or unstrained material property.

Strain for composite electrode film.—We treat the composite electrode film as a homogenized isotropic continuum whose properties can nevertheless vary locally. Strain (here θ) and other properties without subscript a are intended to apply to this homogenized film. For simplicity, we neglect viscoelasticity or creep, fatigue, fracture, delamination, strain-hardening, and thermal behaviors.

Let us consider a Cartesian coordinate system where x is the direction for the net flow of electrical current, i.e. normal to the film. The two other orthogonal coordinates (denoted y) are tangential to the film and are equivalent to each other. Consistent with Duhamel-Neumann Law, the total strain in the film can be expressed as a combination of elastic, plastic, and chemical deformations:

$$\begin{bmatrix} \theta_x \\ \theta_y \end{bmatrix} = E^{-1} \begin{bmatrix} 1 & -2\nu \\ -\nu & 1 - \nu \end{bmatrix} \begin{bmatrix} \sigma_x \\ \sigma_y \end{bmatrix} + \begin{bmatrix} 1 \\ -\frac{1}{2} \end{bmatrix} \frac{1-\nu}{1-2\nu} \theta_p + \begin{bmatrix} 1 \\ 1 \end{bmatrix} \theta_* \quad [3]$$

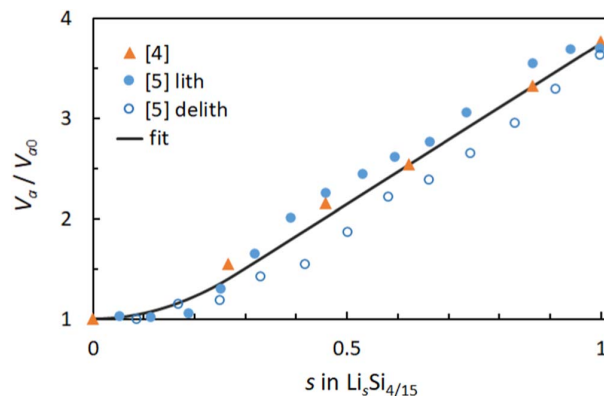


Figure 1. Volume evolution of amorphous Li-Si alloy with state of lithiation, showing experimental points from the Dahn group^{4,5} and a piecewise fitted curve.

where σ is stress, E is Young's elastic modulus, and ν is Poisson's ratio. The first term on the right of the equality represents elastic strain. The next term containing combination $\frac{1-\nu}{1-2\nu} \theta_p$ represents plastic deformation if the yield strength is exceeded. The final term containing θ_* represents isotropic chemical strain. At this point, the values of θ_p and θ_* are arbitrary and expressions will be given later. However, the comparative x and y elements of plastic strain are formulated to preserve volume, known as zero dilatancy in flow plasticity theory.³⁴ We follow the standard convention that positive σ and θ values represent tension/expansion and negative values represent compression/contraction.

Let us next stipulate that tangential strain is negligible, $\theta_y = 0$. This closure relation is a simplification of a more complicated mechanical coupling—and sometimes nexus of failure—between the porous electrode film and the metallic current collector to which it is laminated.^{35–37} Provided the current collector is not too thin and no delamination occurs, its much larger elastic modulus means it will constrain $\theta_y \approx 0$ for the film, and indeed this has been observed experimentally.³⁸ Additionally, the cell format, such as a spiral winding, could contribute to a tangential strain constraint on the film.

Subsequent inversion of Eq. 3 gives an expression for film stresses:

$$M^{-1} \begin{bmatrix} \sigma_x \\ \sigma_y \end{bmatrix} = \begin{bmatrix} 1 \\ \frac{1}{2}(k-1) \end{bmatrix} \theta_x - \begin{bmatrix} 1 \\ -\frac{1}{2} \end{bmatrix} \theta_p - \begin{bmatrix} k \\ k \end{bmatrix} \theta_* \quad [4]$$

From this equation, we can express film normal strain in terms of elastic, plastic, and chemical components, by design in a form considerably simpler than first seen in Eq. 3:

$$\theta_x = M^{-1}\sigma_x + \theta_p + k\theta_* \quad [5]$$

where $-\sigma_x$ is the stack pressure. M is the so-called longitudinal or constrained elastic modulus for the film:

$$M = \frac{1-\nu}{(1-2\nu)(1+\nu)} E \quad [6]$$

Dimensionless property k is given by

$$k = \frac{1+\nu}{1-\nu} \quad [7]$$

E and ν for composites are further described in Eqs. 22–26.

Due to lateral confinement, the superficial area of the electrode is constant. Local volume V of electrode per mole of host material is determined solely by normal strain:

$$\frac{V}{V_0} = 1 + \theta_x = 1 + M^{-1}\sigma_x + \theta_p + k\theta_*, \quad [8]$$

Material volume fractions.—Material volume fractions in the composite film (here ϵ_i), including the porosity, can be determined from a conceptual series of mixing and strain processes for the film. The active material itself is not an ideal mixture, meaning that volume is not conserved during the mixing of its constituent Si and Li elements. The model does conserve solid volume during the next step of mixing the electrode constituents (active material, carbon additive, and binder), a standard assumption when computing densities of alloys and composites in materials science. Finally, solid and overall volumes are not conserved during lithiation-induced strain processes of the electrode, leading to changes in film porosity and thickness.

The volume fraction of electrochemically functional active material is given by

$$\epsilon_a = \frac{\epsilon_{a0} (V_a/V_{a0})}{(V/V_0)} \quad [9]$$

where $\epsilon_{a0} = V_{a0}/V_0$. The volume fraction of inert solid, which includes carbon, binder, and active material that is isolated or deactivated, is likewise given by

$$\epsilon_n = \frac{\epsilon_{n0}}{(V/V_0)} \quad [10]$$

This equation treats the aggregated inert solid as incompressible, meaning its skeletal density does not change during cell operation. Finally we determine porosity ϵ by difference:

$$\epsilon = 1 - \epsilon_a - \epsilon_n \quad [11]$$

The above algebraic approach is consistent with³³ but differs from some prior work where porosity is determined by its own continuity-based differential equation.^{2,21,24} While either approach can be acceptable, one must avoid the pitfalls of failing to account for electrode strain and inert solids volume. Also, one must not confound pore or void volume with liquid electrolyte volume as they have different physical dependencies and are decoupled by the presence of the electrolyte reservoir (see Eqs. 42 and 43).

The needed initial or strain-free volume fractions can be determined readily from experiment and the following equations.

$$\begin{aligned} \epsilon_{a0} &= (1 - \epsilon_0) \phi_{a0} \\ \epsilon_{n0} &= (1 - \epsilon_0)(1 - \phi_{a0}) \\ \epsilon_0 &= 1 - \frac{\rho_0}{\rho_s} \\ \rho_s &= \left(\frac{w_a}{\rho_a} + \frac{w_b}{\rho_b} + \frac{w_c}{\rho_c} \right)^{-1} \\ \phi_{a0} &= \frac{\epsilon_{a0}}{\epsilon_{a0} + \epsilon_{n0}} = \frac{w_a \rho_s}{\rho_a} \chi_a \end{aligned} \quad [12]$$

In the first two lines, we separate ϵ_{a0} and ϵ_{n0} into porosity-dependent and porosity-independent terms and thereby introduce some new quantities that require discussion. Note that any of these properties could vary with position x , for instance in a multilayer or porosity-gradient electrode.³ Furthermore, film thickness and hence ϵ_0 may be adjusted for electrolyte-induced swelling or the cumulative strain of previous cycles. ρ_0 is the initial density of the porous dry film, measured globally from solids loading and thickness of the film, or locally by tomography or sectioning. ρ_s is all-solid skeletal density, determined from dry mass fraction w_i and skeletal density ρ_i of the constituents, namely pristine active material (a), polymeric binder (b), and conductive carbon additive (c).

ϕ_{a0} is the initial solid volume fraction of functional active material and serves as a key determinant of electrode behavior. The nominal amount of active material ($w_a \rho_s / \rho_a$ in Eq. 12) is

adjusted by χ_a , the fraction of active material that is electrochemically functional. For instance, if the Si active material has 2150 mAh/g measured capacity at small C-rates and excess lithium inventory, then $\chi_a = 2150/3578 = 0.6$ (see Eq. 60). Although not done here, χ_a could be made to vary with time or cycling to account for ongoing degradation of active material.

Plastic strain.—Next, we consider how to calculate plastic strain θ_p . We assume a linear Drucker-Prager yield criterion, which allows for a different onset of yield under tension vs. compression.³⁹ It is suitable for soils, foams, and polymers, and thus by extension for particle-based electrodes. The yield function describing allowable stress states in σ_x and σ_y is

$$F_Y = |\sigma_x - \sigma_y| + b_Y(\sigma_x + 2\sigma_y) - \sigma_Y \leq 0 \quad [13]$$

where σ_Y is the harmonic mean of compressive and tensile yield strengths and $0 \leq b_Y < \frac{1}{2}$ is a related asymmetry parameter. If Eq. 13 is separately applied to hypothetical uniaxial and biaxial stress experiments, it leads to the respective constraints

$$\begin{aligned} -\frac{\sigma_Y}{1-b_Y} &\leq \sigma_x \leq \frac{\sigma_Y}{1+b_Y} \quad \text{if } \sigma_y = 0 \\ -\frac{\sigma_Y}{1-2b_Y} &\leq \sigma_y \leq \frac{\sigma_Y}{1+2b_Y} \quad \text{if } \sigma_x = 0 \end{aligned} \quad [14]$$

where the stress limits on the left are for compression, and on the right for tension, each showing the effect of b_Y . The difference between the uniaxial and biaxial results shows that effective yield limits for a film depend on how it is confined.

Neither constraint in Eq. 14 exactly applies to the present electrode model. Instead, we convert Eq. 13 into a strain form upon dividing each term by modulus M :

$$F_Y^* = |\theta_D| + b_Y \theta_V - \theta_Y \leq 0 \quad [15]$$

With help from Eq. 4, the needed deviatoric, volumetric, and yield strains are respectively

$$\begin{aligned} \theta_D &= M^{-1}(\sigma_x - \sigma_y) = \frac{1}{2}(3-k)(M^{-1}\sigma_x + k\theta_*) - \frac{1}{2}k\theta_p \\ \theta_V &= M^{-1}(\sigma_x + 2\sigma_y) = k(M^{-1}\sigma_x + \theta_p) - (3-k)k\theta_* \\ \theta_Y &= M^{-1}\sigma_Y \end{aligned} \quad [16]$$

Yield criterion Eq. 15 may be solved for the plastic strain by use of $|\theta_D| = \theta_D \operatorname{sgn}(\theta_D)$ and Newton's root-finding method. Notably, because of the inequality in Eq. 15, θ_p is a lagging and path-dependent variable, prone to stops and starts. Here we cast the expected iteration for θ_p instead as a differential equation, making it easier to compute in a P2D model:

$$\tau_p \frac{\partial \theta_p}{\partial t} = \frac{2 \operatorname{sgn}(\theta_D) \max(0, F_Y^*)}{k [1 - 2b_Y \operatorname{sgn}(\theta_D)]} \quad [17]$$

Parameter τ_p controls numerical stability vs. rate of convergence; a reasonable value is the average integration time step. Alternatively, τ_p can be thought of as a viscoplastic relaxation time constant and determined accordingly.

As described below, E and thus M are functions of material volume fractions. There are limited measurements of yield strength for porous electrodes, as compared to elastic modulus. We reasonably assume that σ_Y has a compositional dependence similar to M and therefore treat θ_Y and b_Y as constants for the film. Because of the granular nature of Li-ion electrodes, we expect $\theta_Y \ll 1$ and compressive yield strength to greatly exceed tensile yield strength, leading to b_Y being close to but less than $\frac{1}{2}$.

Chemical strain and swelling coefficients.—Weidner and coworkers defined swelling coefficient g as the exponent describing the fractional change of electrode volume V resulting from a fractional

change in active particle volume V_a :²⁴

$$\frac{V}{V_0} = \left(\frac{V_a}{V_{a0}} \right)^g \quad [18]$$

The value of g characterizes the rearrangement of particles in the composite upon their expansion, thereby impacting porosity vs. electrode thickness. Such a closure relationship is clearly needed. However, the above use of g does not—as we intend to do—explicitly account for external stress, plastic deformation, lateral film confinement, the fraction of active material in the electrode, and particle packing limits. Because of the complexity hiding inside of g , its value could change with lithiation and is not readily predicted a priori.⁴⁰

We instead propose that chemical strain in the electrode film depends on active volume according to

$$\theta_* = \left(\frac{V_s}{V_{s0}} \right)^{g/3} - \left[1 + h^5 \left(\frac{V_s}{V_{s0}} - 1 \right)^5 \right]^{-1} \quad [19]$$

Exponent g continues as a swelling coefficient and is now joined by h . The two main terms in Eq. 19 were empirically developed to be capable of fitting the multiple electrode lithiation experiments shown in Figs. 2 and 3, and be general enough to allow extension of the model in future cases of mixed active materials. V_s is the molar volume of combined solids. Ratio V_s/V_{s0} accounts for the volume expansion of functional active material but also for the diluting effect of non-expanding inerts:

$$\frac{V_s}{V_{s0}} = \phi_{a0} \left(\frac{V_a}{V_{a0}} \right) + (1 - \phi_{a0}) \quad [20]$$

Let us further compare Eq. 18 to our new approach. If we assume, as is frequently the case, that the electrode is operating at either the compressive or tensile yield limit (i.e. $F_y^* = 0$ in Eq. 15), then our model produces by elimination of θ_p the analytic result

$$\frac{V}{V_0} = 1 + 3\theta_* + \frac{3M^{-1}\sigma_x - 2\theta_y \text{sgn}(\theta_D)}{k[1 - 2b_y \text{sgn}(\theta_D)]} \quad [21]$$

It can be shown that the combination of Eqs. 19–21 reduces to the previously posited Eq. 18, in the absence of external stress ($\sigma_x = 0$) and under modest amounts of volume change ($\theta_y \ll \theta_* \ll 1$). This suggests that the old and new models could equivalently describe an electrode with modest expansion, such as an LCO cathode.⁴⁰ In this case, the old and new g values will differ by a factor of ϕ_{a0} but otherwise function the same. This equivalence breaks down, however, at larger expansions characteristic of graphite and Si electrodes or when σ_x is significant. Equation 21 is not intended to be a replacement for Eq. 8 in the model, but rather to reveal here typical and approximate model behavior. During transitory conditions of pure elastic deformation, the electrode will operate between the limits generated by $\text{sgn}(\theta_D) = \pm 1$, such that Eq. 21 provides a set of bounds for operating conditions. The volume hysteresis loop in upcoming Fig. 4d illustrates such limits.

Figure 2 compares results from Eqs. 19–21 to experimental data from multiple literature sources employing electrochemical dilatometry to determine electrode thickness changes, and requires some discussion. LCO and graphite electrodes are given as points of comparison.^{40,41} We selected data for silicon electrodes with a high mass fraction of silicon, namely $w_a \geq 0.5$.^{38,41–44} For each source, we used data from the second or third lithiation cycle when available, and reset SoL and strain to zero at the beginning of that cycle. Equations 20 and 60 were used to re-cast the original running capacity data, first as SoL and then as $V_s/V_{s0} - 1$, the abscissa of the plot. Compiled ϕ_{a0} values, which describe the amount of functional active material (Eq. 12), are given in the figure. The respective binders are also specified for Si electrodes and include Nafion (Naf), sodium alginate (SA), CMC, lithium-substituted polyacrylic acid (LiPAA), and polyimide (PI) binders.

Figure 2 shows a wide variety in expansion behavior of Si electrodes, complicated by binder type, Si type, initial volume fractions of constituents, and cycling history. And this is setting aside possible experimental error when there is compensation (or not) for volume change in the counter electrode. This makes unambiguous fitting of the entire data set difficult. Nevertheless, Eqs. 19–21 (here assuming $\sigma_x \approx 0$ and $\theta_y \approx 0$) describe reasonably well not only the Si electrodes but also the LCO and graphite electrodes.

The first term in Eq. 19 generates a nearly linear fitting curve on the log-log plot of Fig. 2 where g controls the position of the curve at

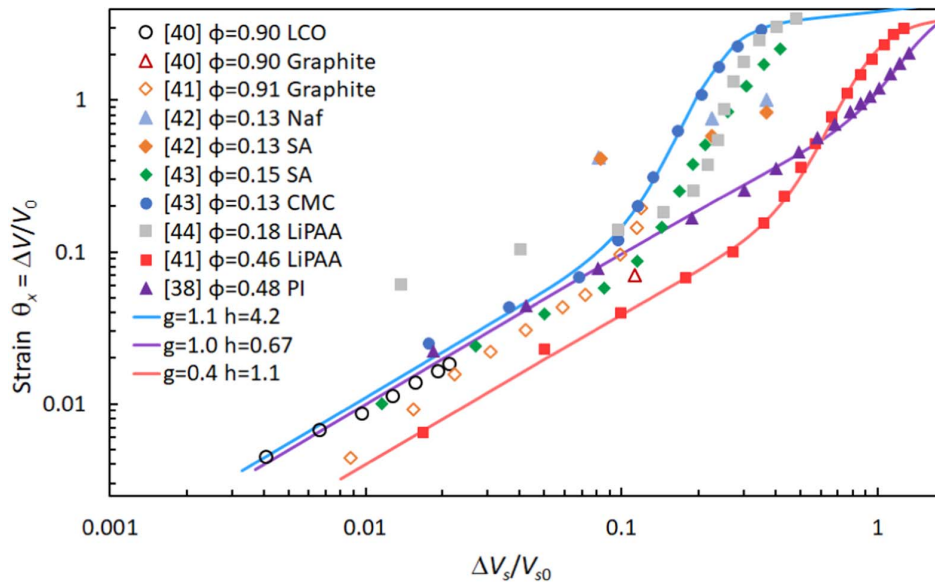


Figure 2. Electrode strain in response to lithiation-induced solid expansion, from experimental values for LCO and graphite (open symbols)^{40,41} and for silicon mixed with various binders (closed symbols).^{38,41–44} Experimental ϕ_{a0} values are indicated. Example fits (lines) from Eqs. 19–21 with indicated swelling coefficients are presented for three of the experimental series. Note the logarithmic axes.

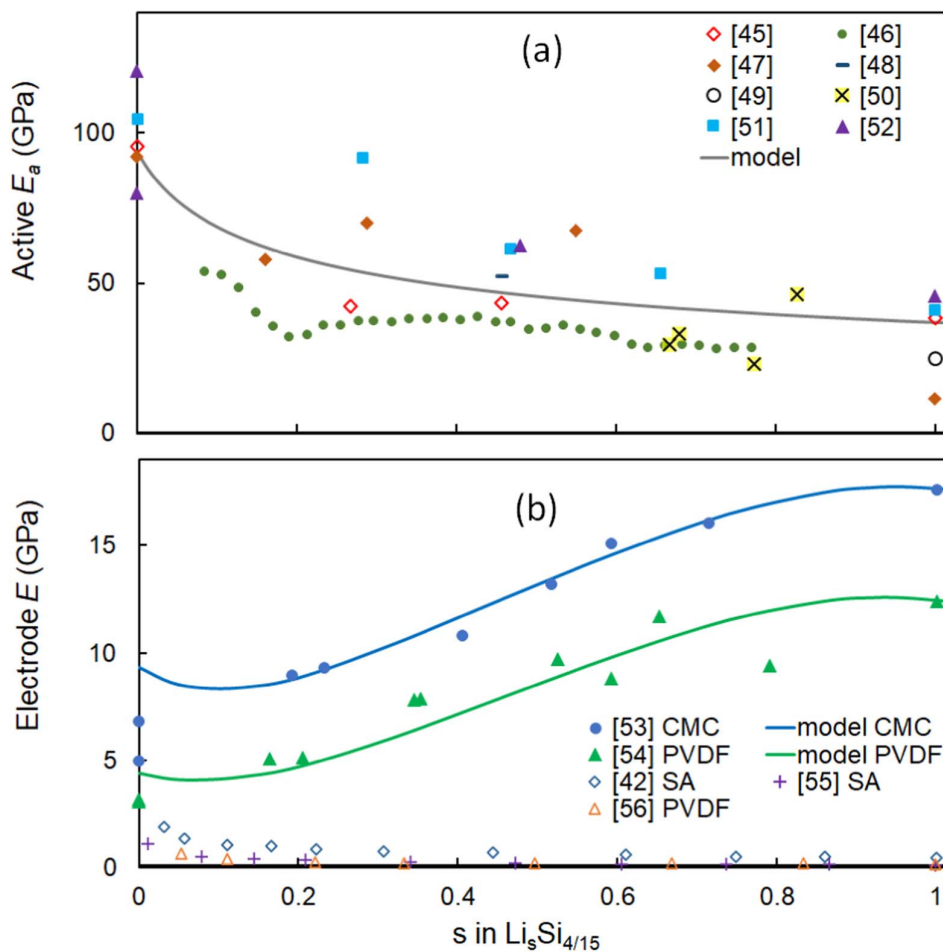


Figure 3. Elastic modulus variation with state of lithiation by different studies^{42,45–56} for (a) Li-Si alloy and (b) porous Si-based electrodes. Model curves are described in the text. In (b) the top two experimental series use nanoindentation while the bottom three series use cantilever experiments.

small degrees of lithiation. The second term in Eq. 19 and an appropriate h value are needed to match the observed departures from linear behavior at large degrees of lithiation. The point of departure for a given electrode corresponds to a minimum in porosity or maximum in solid packing fraction. This can be compared to the maximum volume fraction for random or jammed packings of uniform spheres and for close-packed crystals.³⁰ The present model is therefore capable of describing the jamming of active and inert particles that leads to a constraint on volume fractions. Coefficient h indicates the rapidity with which particle packing limitations become significant upon lithiation; it varies from one electrode to another but is partially characterized by an inverse dependence on ϕ_{a0} .

The ranges of swelling coefficients describing most of the observed Si electrodes are $0.4 < g < 1.1$ and $0.21\phi_{a0}^{-1} < h < 0.55\phi_{a0}^{-1}$. Given these uncertainties, we recommend using $g = 0.7$ and $h = 0.21\phi_{a0}^{-1}$ to conservatively describe a silicon electrode in the absence of cell-specific dilatometry data; these values are used in our primary model below.

Elastic modulus.—The porous electrode consists of active material, carbon, binder, and pores, each with its own mechanical properties and volume fraction. We seek a method to coarse-grain or homogenize these constituents to get a composite electrode elastic modulus. Recall that constrained modulus M for the electrode is determined from E by means of Eq. 6.

Figure 3 summarizes reported values of elastic modulus during lithiation of (a) Si active material and (b) corresponding porous electrodes. For the active material there are both simulation⁴⁵ and experimental^{46–52} data. In general, a softening in modulus is observed upon Li insertion into Si, but uncertainties are large and no unequivocal trend is suggested by the literature points in Fig. 3a. For purposes of this work, a model curve is used to approximate and follow the general trend:

$$E_a = [sE_{a1}^\ell + (1-s)E_{a0}^\ell]^{1/\ell} \quad [22]$$

where $E_{a0} = 94$ GPa, $E_{a1} = 37$ GPa are endpoints, and exponent $\ell = -3$ controls the curve shape.

Literature on the elastic modulus of foams and other cellular materials suggests that at high density (i.e. ϵ generally less than 0.5), elastic modulus depends on porosity according to

$$E = E_s (1 - \epsilon)^{1/m} \quad [23]$$

where E_s is the all-solid modulus. While the exponent is observed to have a range of possible values depending on the microstructure, $m \approx 0.5$ is commonly accepted for open-cell foams.^{57,58} On the other hand, $m \approx 0.25$ matches simulation data for a composite of overlapping solid spheres.⁵⁷

Here we propose a generalized rule of mixtures to homogenize or coarse-grain the elastic modulus of a porous film from moduli for active (a) and inert (n) constituents:

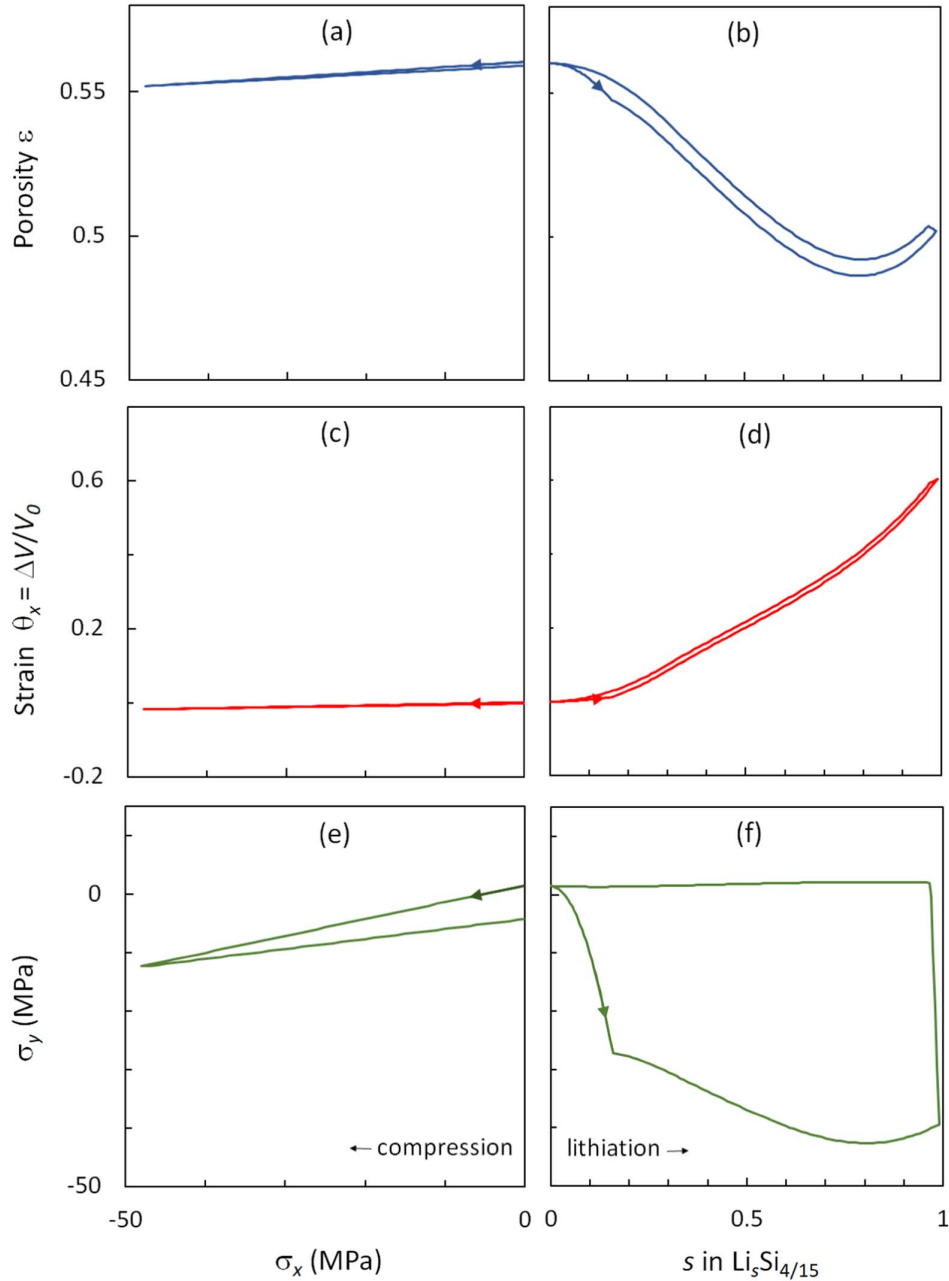


Figure 4. Calculated Si electrode porosity, volume change, and in-plane stress under conditions of (a, c, e) no lithiation and varying compressive normal stress, and (b, d, e) no normal stress and varying lithiation. The hysteresis loops, each with an arrow indicating direction, are due to plastic yielding in the film.

$$E = (\epsilon_a E_a^m + \epsilon_n E_n^m)^{1/m} \quad [24]$$

The final constituent, pore volume, would be included in the sum in like manner, except that voids have zero elastic modulus and the term is removed. As with Eq. 23, exponent m depends on microstructure and is determined empirically. In a conventional rule of mixtures, one uses either $m = 1$ to make the so-called Voigt modulus (arithmetic mean) or $m = -1$ to make the so-called Reuss modulus (harmonic mean).⁴³ In Eq. 24, however, $0 < m \leq 1$ is allowed, while $m \leq 0$ is not allowed because of the zero modulus of the implied pore volume. In the field of geological reservoir modeling, a formula equivalent to Eq. 24 has been used to

homogenize the permeability of rock formations; this is known as power-law averaging.⁵⁹

The advantages of Eq. 24 are its simplicity, generality when constituent volume fractions dynamically change, and correct behavior at limits $\epsilon_i \rightarrow 0, 1$. It does not require one to separately estimate E_s . However, if this is desired, a combination of Eqs. 11, 23 and 24 implies that

$$E_s = \left(\frac{\epsilon_a E_a^m + \epsilon_n E_n^m}{\epsilon_a + \epsilon_n} \right)^{1/m} \quad [25]$$

which is a reasonable approach to describe an all-solid mixture by means of a volume-weighted average. Indeed, the form of Eq. 25

could be used to estimate E_n itself from its sub-constituents carbon, binder, and dead active material (see Eq. 12).

Two main factors determine whether the elastic modulus of a Si-based electrode increases or decreases with lithiation: the elastic modulus of Li-Si alloy that decreases upon lithiation (Eq. 22), and the porosity ϵ of the electrode that controls density and hence composite elastic modulus (Eq. 24). To sort out these two factors, Fig. 3b includes two types of measurements reported in the literature for the elastic modulus of Si composite electrodes. The first group by Wang et al. utilized nanoindentation and generated larger elastic moduli with an increasing trend with lithiation.^{53,54} An increase in E is consistent with a decrease in porosity. The second group used the curvature of an electrode cantilever, and generated smaller elastic moduli with a decreasing trend with lithiation.^{42,55,56,60} Our elasticity and porosity models are more consistent with the results by Wang et al. We also judge that the cantilever method, in contrast to nanoindentation, is less accurate because the fitting equation does not consider plastic yielding in the electrode film, even though it is experimentally observed. In general, failure to account for plastic strain would produce an apparent elastic modulus that is smaller than the true value. Equation 24 is used to produce the two model curves for Si composite electrodes in Fig. 3b, which show satisfactory agreement with the experiment given the uncertainties in measured elastic moduli and volume fractions. A consistent fit was produced by microstructure exponent $m = 0.37$, which is used in the remainder of this work. Needed fractions ϵ_a and ϵ_n for the model curves were estimated from w_i , ρ_i , and ϵ data provided by Wang et al.^{53,54} The inert fractions were taken to have $E_n = 10$ GPa for the CMC binder and $E_n = 6$ GPa for the PVDF binder. The maximum in E for each model curve at a high degree of lithiation is due to the particle-packing constraint in Eq. 19 with $h = 0.21\phi_{a0}^{-1} \approx 0.48$.

A reasonable approximation for the Poisson's ratio of porous layers can be derived from simulation data for overlapping solid spheres:⁵⁷

$$\nu = \nu_s + \left(\frac{1}{7} - \nu_s\right) \min\left(1, \frac{9}{4}\epsilon\right) \quad [26]$$

All-solid effective values are $\nu_s \approx 0.27$ for the Si electrode and $\nu_s \approx 0.4$ for the polyolefin separator. Equation 26 is part of the set of mechanical equations (including Eqs. 6–11) that must be solved iteratively.

Electrode mechanical response.—In Fig. 4 we examine how a representative porous Si electrode might mechanically respond to perturbations, using the set of relationships proposed above. We assume the following constants: $\phi_{a0} = 0.3$, $\epsilon_0 = 0.56$; $g = 0.7$, $h = 0.7$, $\theta_Y = 0.001$, $b_Y = 0.45$, $m = 0.37$, $E_n = 11$ GPa, and $\nu_s = 0.27$. Figure 4 shows iteratively calculated film porosity, normal strain (i.e. volume change), and tangential stress for two cases: where σ_x is varied (producing compression) while lithiation or chemical strain is zero, and where spatially uniform lithiation is changed in the electrode, while external stress is zero. In each case, a full cycle of stress or lithiation is done to show the hysteresis loop caused by plastic yielding.

The properties change nearly linearly and as expected under the action of normal stress in Fig. 4 panels a, c, and e. Prominent nonlinear and hysteretic effects appear under varying lithiation in panels b, d, and f. In all cases, plastic deformation begins quite early after perturbation due to the small value of yield strain for the porous electrode. The upward trend in thickness (panel d) is always observed experimentally.^{43,54} Panel b is notable for the predicted minimum in the porosity at an intermediate SoL. As shown in panel d (and repeatedly in the experiments of Fig. 2), there is a transition in the slope of the electrode strain at high degrees of lithiation. This transition mathematically corresponds to a minimum in porosity. A related physical explanation is that porosity cannot continue to decrease when active material particles make rigid contact and

otherwise become jammed, requiring greater electrode strains to accommodate particle volume increases. The transition point varies from cell to cell, with its propensity given by swelling coefficient h . This non-monotonic porosity behavior has been observed to depend on type of polymer binder.⁴²

As a further confirmation of electrode mechanical model predictions, Fig. 4f shows a distinctive hysteresis loop for tangential or in-plane stress that is a remarkable semi-quantitative match to in situ measurements of this property from independent studies of three different electrodes.^{42,43,61} The mechanical model here thus confirms the pervasive plastic deformation of Si electrodes under nearly all operational conditions.

Separator mechanical response.—The mechanical description of the separator must be reasonably accurate because the separator is typically much more compliant than the electrode film and therefore has a significant effect on cell stress-strain response. The principal mechanical relationships given above are applicable to the separator layer, with the following noted alterations. First, the absence of active material is an obvious change and leads to $\epsilon_a = \epsilon_{a0} = \phi_{a0} = \theta_s = 0$. Second, unlike the electrode, mechanical properties are typically uniform across the separator. Third, because the separator is not laterally constrained by a current collector, it is subject to $\sigma_y = 0$ rather than $\theta_y = 0$. Fourth, for simplicity in describing yield in the separator, we let $b_Y = 0$. The following primed equations for the separator therefore replace the corresponding original equations for the electrode.

$$\theta_x = E^{-1}\sigma_x + \theta_p \quad [5']$$

$$\frac{V}{V_0} = (1 + E^{-1}\sigma_x + \theta_p) \left(1 - \nu E^{-1}\sigma_x - \frac{1}{2}\theta_p\right)^2 \quad [8']$$

$$\tau_p \frac{\partial \theta_p}{\partial t} = \text{sgn}(\sigma_x) \max(0, E^{-1}|\sigma_x| - \theta_Y) \quad [17']$$

Eqs. 10, 11, 24, and 26 continue to be used unmodified.

Figure 5 shows how these simple equations reasonably describe the nonlinear and path-dependent compressive stress-strain behavior of a Celgard 3501 membrane.⁶² The fitting parameters are given in Table I. Note the permanent plastic deformation that occurs for $\sigma_x < -20$ MPa and is obvious upon stress unloading. A comparison of Figs. 5 to 4c shows that, as expected, the separator is significantly more compliant than the electrode film.

Geometry and stress evolution in the cell.—A half-cell sandwich consists of multiple layers and dependent variables as depicted in Fig. 6. The electrochemical model here comprises only three layers: porous anode, separator, and Li foil. On the other hand, the cell mechanical model takes into account all layers including current collectors and casing.

In the mechanical model, the casing layer is an inert material whose thickness and stiffness can be adjusted to imitate the external stress-strain response generated by the actual packaging. For purposes of the model, the casing layer elastically accommodates the strain in the remaining layers such that the total thickness of all layers (including the casing) is constant:

$$\sum_j (L_j - L_{0,j}) = 0 \quad [27]$$

where L_j is the thickness of layer j in the cell sandwich. For convenience in many equations below, subscript j is removed from quantities like L , which are nevertheless understood to vary on a layer-by-layer basis.

Electrochemically active layers, e.g., the Si anode, have a position-dependent strain that follows Eq. 5. The elastic, plastic, and chemical strains are interdependent functions of the local degree of lithiation. For non-active layers, e.g., separator, current collectors,

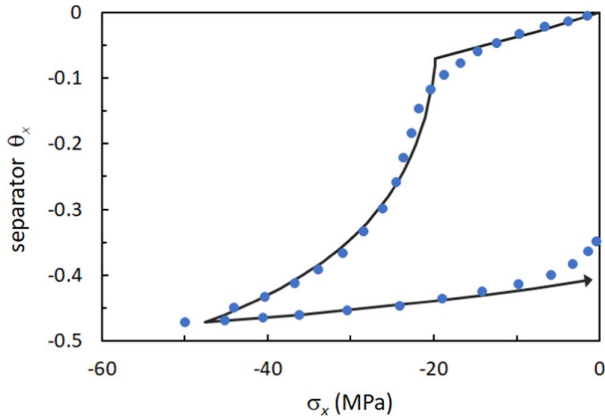


Figure 5. Normal strain as a function of normal compressive stress in a porous separator. Experimental points for Celgard 3501⁶² and model curve, with an arrow indicating path direction due to plastic yielding in the film.

and casing, Eq. 5 does not have a chemical strain component, and θ_x is uniform within the layer.

The partial differential equations (PDEs) for material conservation are solved on dimensionless strain-free coordinates in the electrode normal (x^*) and particle radius (r^*) directions. This allows for a static mesh to be used for all computations. Local strain θ_x and initial layer thickness L_0 lead to a Jacobian-like mapping or material deformation gradient that allows us to convert between unstrained and dimensionless position x^* and strained actual position x :

$$\frac{\partial x}{\partial x^*} = L_0(1 + \theta_x) = L_\theta \quad [28]$$

L_θ is a convenient grouping that is used repeatedly below. Equation 28 must be integrated, along with other PDEs during the course of a battery simulation, to determine x :

$$x = \int_0^{x^*} L_\theta dx^* \quad [29]$$

And when the integration is across an entire layer then the strained layer thickness can be determined:

$$L = \int_0^1 L_\theta dx^* = \langle L_\theta \rangle_1 \quad [30]$$

where the notation $\langle \dots \rangle_1 = \int_0^1 \dots dx^*$ is used here and below. As shown in Fig. 6, coordinate x^* experiences a unit change across each layer in the cell, e.g., from 0 to 1 or 1 to 2. For simplicity in presenting the above integral, we assumed the anode layer where $0 \leq x^* \leq 1$.

We need to compute σ_x , the normal stress or negative stack pressure at a given time. Combining Eqs. 8, 27, and 30 gives

$$\sum_j L_{0,j} \langle M^{-1} \sigma_x + k\theta_* + \theta_p \rangle_j = 0 \quad [31]$$

where M is used for generality but becomes E for non-active layers. Next σ_x is factored out because it is the same for each layer j .

$$\sigma_x = - \frac{\sum_j L_{0,j} \langle k\theta_* + \theta_p \rangle_j}{\sum_j L_{0,j} \langle M^{-1} \rangle_j} \quad [32]$$

This global σ_x value is cycled back into Eq. 5 to compute layer strains. We also need velocity v_x to account for the advection of the solids and electrolyte due to strain:

$$v_x = \frac{\partial x}{\partial t} \Big|_{x^*} = \int_0^{x^*} \frac{\partial L_\theta}{\partial t} \Big|_{x^*} dx^* \quad [33]$$

Conservation of Li in electrolyte.—Now we turn to the electrochemical model. The significant volume change of Si active material necessitates changes to conventional P2D model equations.² Here we develop the conservation equation for Li in the electrolyte.

Because porosity and layer thicknesses are changing, we must consider the fate of the liquid electrolyte. Specifically, these processes will necessarily cause incompressible electrolyte to squeeze out from the pores to adjacent pores or to outside the electrode area, and vice versa. To deal with this, we utilize the concept of a liquid-phase reservoir, an idea anticipated but not realized in prior modeling studies.^{21,63} Such a reservoir has a

Table I. Mechanical and electrochemical parameters used for the baseline P2D model.

	Silicon	Separ	Li foil	CCs	Casing	
ϵ_0	0.56 ^{a)}	0.55 ^{c)}	0	—	—	
ϕ_{a0}	0.275	0	1	—	—	
g	0.70	—	—	—	—	
h	0.76	—	—	—	—	
L_0	8.5 ^{a)}	25	20	10	100	μm
E_a	Eq. 22	—	3 ^{b)}	—	—	GPa
E_n	11	7.5 ^{c)}	—	130	0.01,100	GPa
m	0.37	0.23 ^{c)}	—	—	—	
ν_s	0.27	0.40	—	—	—	
θ_Y	0.001	0.068 ^{c)}	—	—	—	
b_Y	0.45	0	—	—	—	
τ_p	0.1	0.1	—	—	—	s
γ	3	3	—	—	—	
κ_s^{int}	300 ^{d)}	0	—	—	—	S m^{-1}
R_{a0}	40 ^{a)}	—	—	—	—	nm
D_a	$1 \cdot 10^{-18\text{e)}$	—	—	—	—	m^2s^{-1}
i_0^{ref}	0.024 ^{a)}	—	12.6 ^{d)}	—	—	A m^{-2}
C_{e0}	1000	1000	1000	—	—	mol m^{-3}
C_{a0}^H	310970	—	—	—	—	mol m^{-3}

Value derived from ^a 67, ^b 74, ^c 62, ^d 21, ^e 20.

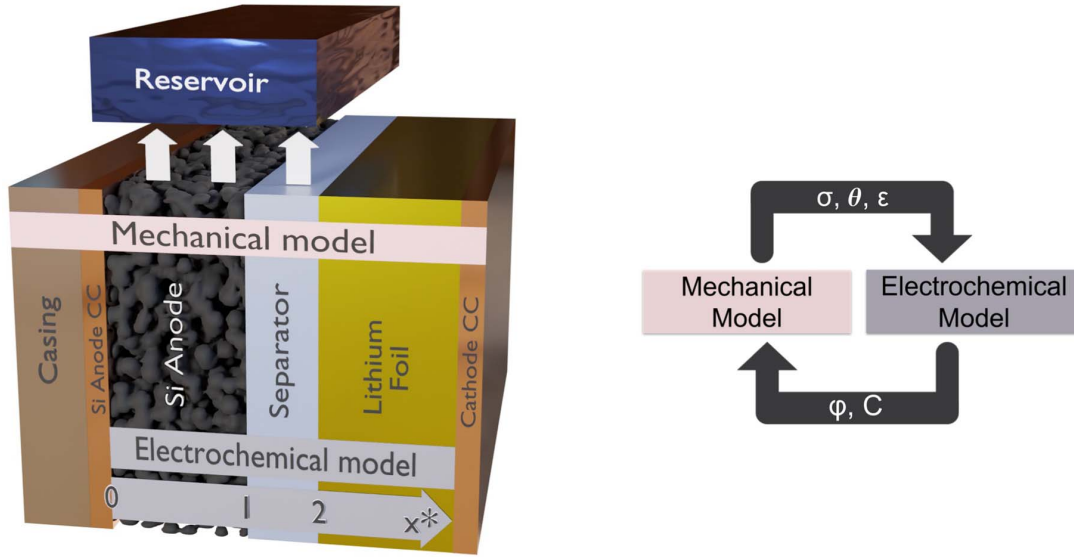


Figure 6. Model schematic. (left) Mechanical and electrochemical models comprise different layers of the cell sandwich and are solved in normal direction x^* . The electrolyte is exchanged with a reservoir through a source term. (right) Dependent variables in each model are solved iteratively.

physical analog in cell designs. For instance, it can be assumed that excess electrolyte is stored in the electrode periphery or cell header space. Figure 6 illustrates the relationship of the liquid reservoir to other cell elements. We wish to continue using a 1D electrolyte conservation law while treating flows to and from the reservoir in an efficient volumetrically averaged manner. This is done through a combination of an advection term for liquid motion in the normal direction and a source term. Our use of the source term sidesteps a complicated solution to hydrodynamic equations in the pores. Without the term, large amounts of Li^+ ions seemingly are gained or lost from the cell during cycling, a clearly inaccurate result.

The 1D electrolyte conservation or continuity equation is

$$\left. \frac{\partial(C_e \epsilon)}{\partial t} \right|_x = -\frac{\partial N_e}{\partial x} + a_a j_a^{\text{rxn}} (1 - t_+^0) + F_{\text{res}} \quad [34]$$

where C_e is electrolyte concentration such that $C_e \epsilon$ has units moles per volume of electrode. The right side has the customary “divergence of the flux” term as well as two source terms. The first source term is for the distributed electrochemical reaction where a_a is reactive area per electrode volume, j_a^{rxn} is the rate of surface reaction, and t_+^0 is a constant lithium-ion transference number. In contrast to the reactive term, the reservoir source term, F_{res} , is present in both separator and anode layers.

For computational convenience the conservation equation is solved on the dimensionless strain-free coordinate x^* (Fig. 6). We must therefore refashion Eq. 34 into

$$\left. \frac{\partial(C_e \epsilon)}{\partial t} \right|_{x^*} = \frac{v_x}{L_\theta} \frac{\partial(C_e \epsilon)}{\partial x^*} - \frac{1}{L_\theta} \frac{\partial N_e}{\partial x^*} + a_a j_a^{\text{rxn}} (1 - t_+^0) + F_{\text{res}} \quad [35]$$

The time derivative on the left side of Eq. 35 is effectively a *material* derivative because, under the action of strain, fixed position x^* is actually moving with velocity v_x (see Eq. 33). Converting between Eulerian (Eq. 34) and Lagrangian (Eq. 35) time derivatives requires the first term on the right side of Eq. 35.⁶⁴ Lastly, the derivatives in x are converted to derivatives in x^* by the chain rule and Eq. 28.

N_e is the electrolyte planar flux consisting of diffusive and advective terms: $N_e = J_e + v_x C_e \epsilon$. Here we assume that electrolyte naturally advects with the same strain-induced velocity (v_x) as

adjacent solid particles. The Fickian diffusive flux is

$$J_e = -\frac{D_e}{L_\theta} \frac{\partial C_e}{\partial x^*} \quad [36]$$

where D_e is the salt effective diffusivity through the electrode or separator. Its dependence on porosity has been described with a Bruggeman-type equation:

$$D_e = D_e^{\text{int}} \gamma^{-1} \epsilon^{1.5} \quad [37]$$

where D_e^{int} is the intrinsic diffusivity of the electrolyte and $\gamma \approx 3$ is a dimensionless tortuosity-scaling parameter that depends on the layer microstructure.^{65,66}

The boundary conditions for the PDE are

$$\begin{aligned} J_e &= 0 & \text{at } x^* &= 0 \\ J_e &= -j_{\text{foil}}^{\text{rxn}} (1 - t_+^0) & \text{at } x^* &= 2 \end{aligned} \quad [38]$$

where J_e , C_e , and v_x are continuous across adjacent anode and separator layers at $x^* = 1$. The use of J_e rather than N_e at each of the boundaries is due to the boundaries moving at the same velocity as the fluid, in Lagrangian fashion. In the absence of side reactions, conservation of charge requires that the foil surface and distributed electrode reactions balance:

$$j_{\text{foil}}^{\text{rxn}} = -(a_a j_a^{\text{rxn}} L_\theta)_1 = I_{\text{app}} / \mathcal{F} \quad [39]$$

where I_{app} is applied current density and \mathcal{F} is Faraday's constant. Under the assumption of spherical particles, the local reactive area per electrode volume is

$$a_a = \frac{3\epsilon_a}{R_a} \quad [40]$$

where R_a is particle radius.

Spatially integrating Eq. 35 across the anode (1) and separator (2), plus rearrangement and cancellation of terms, leads to a conservation PDE that will be of use below:

$$\left. \frac{\partial}{\partial t} \langle C_e \epsilon L_\theta \rangle_{1,2} \right|_{x^*} = \langle F_{\text{res}} L_\theta \rangle_{1,2} \quad [41]$$

Next, we derive the reservoir term F_{res} , which locally adds or removes electrolyte, such that the salt and solvent species are conserved across the cell. By assuming any *excess* electrolyte stored in the reservoir is negligible (because reservoir concentration remains close to initial or cell-average value C_{e0} , reservoir volume is small compared to the aggregate volume of pores, or both) we remove considerable model complexity and arrive at a minimum viable scheme. Specifically, we constrain average concentration in the anode and separator to its initial value:

$$\langle C_e \epsilon L_\theta \rangle_{1,2} = C_{e0} \langle \epsilon L_\theta \rangle_{1,2} \quad [42]$$

Taking the time derivative of Eq. 42 and combining with Eq. 41 leads to a suitable though non-unique solution to F_{res} throughout the anode and separator layers:

$$F_{\text{res}} = \frac{C_{e0}}{L_\theta} \frac{\partial(\epsilon L_\theta)}{\partial t} \Big|_{x^*} \quad [43]$$

Note that this term describes not only net lateral flow to or from the reservoir but also flow more directly between adjacent layers. For instance, if the anode pore volume is increasing ($F_{\text{res}} > 0$) and the separator pore volume is decreasing ($F_{\text{res}} < 0$), then F_{res} effectively moves electrolyte from the separator to the anode as a secondary type of advection.

When Eq. 43 is substituted into Eq. 35, and N_e is eliminated in favor of J_e , additional consolidation of terms is possible:

$$\epsilon L_\theta \frac{\partial C_e}{\partial t} \Big|_{x^*} = -\frac{\partial J_e}{\partial x^*} + a_a j_a^{\text{rxn}} L_\theta (1 - t_+^0) + (C_{e0} - C_e) \frac{\partial(\epsilon L_\theta)}{\partial t} \Big|_{x^*} \quad [44]$$

This is the final and complete version of the electrolyte conservation equation that accounts for liquid exchange under strain, including with a reservoir.

Conservation of Li in the active material.—Next, we develop the governing equation for Li conservation in the active material particles. Conventional practice in P2D models is to assume the only Li transport mechanism in the solid phase is diffusion in the radial direction, i.e. the pseudo-second dimension. However, here the stored Li also moves by advection in the x and r directions due to particle strain.

We first define the dimensionless radial position in the particle:

$$\begin{aligned} r^* &= r/R_a \\ R_a &= R_{a0} (V_a/V_{a0})^{1/3} \end{aligned} \quad [45]$$

Radial velocity inside the particle is defined as

$$v_r = \frac{\partial r}{\partial t} \Big|_{x^*, r^*} = r^* \frac{\partial R_a}{\partial t} \Big|_{x^*} \quad [46]$$

The above equations imply that particles expand uniformly, assumed here for simplicity.

Lithium conservation in the spherical particles located at x^* is described by

$$\frac{\partial C_a}{\partial t} \Big|_{x^*, r} = -\frac{1}{r^2} \frac{\partial(r^2 N_a)}{\partial r} \quad [47]$$

where C_a is concentration and N_a is molar radial flux. We must transform Eq. 47 in order to solve it on r^* instead of r , i.e. change from an Eulerian to a Lagrangian time derivative:

$$\frac{\partial C_a}{\partial t} \Big|_{x^*, r^*} = v_r \frac{\partial C_a}{\partial r} - \frac{1}{r^2} \frac{\partial(r^2 N_a)}{\partial r} \quad [48]$$

Subsequent manipulations of Eq. 48 are as follows. We replace the flux with diffusive and advective components: $N_a = J_a + v_r C_a$. We replace each r with $R_a r^*$. We eliminate v_r using Eq. 46. After cancellation and regrouping of terms we obtain a final and complete conservation law for Li in the active phase:

$$R_a \frac{\partial C_a}{\partial t} \Big|_{x^*, r^*} = -\frac{\partial J_a}{\partial r^*} - \frac{2J_a}{r^*} - 3C_a \frac{\partial R_a}{\partial t} \Big|_{x^*} \quad [49]$$

with accompanying boundary conditions

$$\begin{aligned} J_a &= 0 & \text{at } r^* &= 0 \\ J_a &= j_a^{\text{rxn}} & \text{at } r^* &= 1 \end{aligned} \quad [50]$$

Fickian diffusive flux is given by

$$J_a = -\frac{D_a}{R_a} \frac{\partial C_a}{\partial r^*} \quad [51]$$

where D_a is diffusivity and in general depends on C_a , though for Li-Si alloy it is not known with a high degree of certainty.⁶⁷ Concentration and stress gradients both contribute to the true diffusive driving force, a chemical potential gradient. But stress inside the particle is nearly completely dependent on C_a . So without any extra effort, an empirically determined D_a naturally incorporates stress-induced diffusion into Fick's Law.^{68,69}

We require \bar{C}_a , the average Li concentration in particles at position x^* , for determining electrode volumetric and mechanical properties such as V_d/V_{a0} in Eq. 45. \bar{C}_a is determined by spherical integration:

$$\bar{C}_a = \frac{\int_0^1 C_a 4\pi r^{*2} dr^*}{\int_0^1 4\pi r^{*2} dr^*} = \int_0^1 3C_a r^{*2} dr^* \quad [52]$$

Or if desired, Eqs. 49, 50, and 52 can be combined to provide a direct PDE for \bar{C}_a :

$$R_a \frac{\partial \bar{C}_a}{\partial t} \Big|_{x^*} = -3j_a^{\text{rxn}} - 3\bar{C}_a \frac{\partial R_a}{\partial t} \Big|_{x^*} \quad [53]$$

A combination of Eqs. 8, 9, 28, and 45 shows that $\epsilon_a L_\theta R_{a0}^3 = \epsilon_{a0} L_\theta R_a^3$. This relationship allows Eq. 53 to be re-expressed as

$$\frac{\partial(\bar{C}_a \epsilon_a L_\theta)}{\partial t} \Big|_{x^*} = -a_a j_a^{\text{rxn}} L_\theta \quad [54]$$

which is used below to demonstrate the model's internal consistency, i.e. conservation of Li.

State of lithiation.—This Section shows how the state of lithiation (SoL or s) and electrode capacity are computed, as particular care must be exercised when strain and porosity variations are introduced into an electrode. SoL is needed for different spatial domains, in each case defined as the ratio of Li stored to the maximum that can be stored in the host, therefore having range 0–1 even for electrodes with diminished capacity. At the particle level, the ratio is expressed as

$$s = \frac{C_a}{C_a^H} = \frac{V_a}{V_{a0}} \frac{C_a}{C_{a0}^H} \quad [55]$$

Host concentration $C_a^H = V_a^{-1}$ is the moles of lithium host sites (in this case Si_{4/15}) per volume of active material. For pristine silicon $C_{a0}^H = V_{a0}^{-1} = 310970 \text{ mol/m}^3$. Note that C_a^H decreases with lithiation, as shown by V_a/V_{a0} increasing with lithiation in Fig. 1.

Because s and V_a/V_{a0} are interdependent, Eq. 55 must be solved simultaneously with Eq. 2 for Si. We thereby obtain a closed-form piecewise solution for both variables in terms of dimensionless concentration C_a^* :

$$s = \frac{V_a}{V_{a0}} C_a^* = \begin{cases} \frac{48}{539} C_a^{*-1} \left(1 - \sqrt{1 - \frac{539}{24} C_a^{*2}} \right), & C_a^* < \frac{48}{245} \\ C_a^* \left(\frac{24}{13} - \frac{77}{13} C_a^* \right)^{-1}, & C_a^* \geq \frac{48}{245} \end{cases} \quad [56]$$

Figure 7 shows s and V_a/V_{a0} from this inversion formula. For determining electrode volumetric and mechanical properties (e.g., V_a/V_{a0} in Eqs. 9, 20, and 45) we use $C_a^* = \bar{C}_a/C_{a0}^H$ in Eq. 56, where \bar{C}_a comes from any of Eqs. 52–54. In contrast, a surface concentration is needed for OCP and kinetic calculations (e.g., Eqs. 61, 66, and 71), and so in those contexts we use $C_a^* = C_{a,r^*=1}/C_{a0}^H$ to compute s from Eq. 56.

Electrode-average SoL is also desirable, in order to report aggregate electrode utilization and compare it to experimental studies. It is defined as the ratio of stored lithium (Q_a) to total host sites (Q_a^H):

$$s_{\text{avg}} = \frac{Q_a}{Q_a^H} \quad [57]$$

These quantities, which have units of charge per superficial area of the electrode, are obtained by integrating or averaging concentrations over the electrode thickness:

$$\begin{aligned} Q_a &= \mathcal{F} \langle \bar{C}_a \epsilon_a L \theta \rangle_1 \\ Q_a^H &= \mathcal{F} C_{a0}^H \langle \epsilon_{a0} \rangle_1 L_0 \end{aligned} \quad [58]$$

State of charge (SoC) is a property comparable to SoL. It is calculated from the amount of charge passed through the cell. We simply time-integrate the applied current density:

$$\text{SoC} = \frac{1}{Q_a^H} \int_0^t I_{\text{app}} dt \quad [59]$$

It can be shown that $\text{SoC} = s_{\text{avg}}$, provided that the same initial conditions are used and there are no parasitic side reactions. The equivalence between Eqs. 57 and 59 is proven by starting with Eq. 54 and integrating with respect to x^* and t to respectively conform to Eqs. 58 and 59, with help from Eq. 39. The equivalence confirms that our governing equations properly conserve Li.

Every electrode, and especially one based on Si, soon achieves less than its theoretical maximum capacity, even when cycled at low C-rates against an excess of lithium. To describe this in an electrochemically consistent manner, we propose the approach given in Eqs. 9–12, namely shifting some portion of active material into the inert category by means of ϕ_{a0} , which in turn depends on fractional capacity $\chi_a < 1$. This is distinct from the *apparent* electrode capacity loss caused by a modest increase in cell impedance or a loss of lithium inventory when forming the solid-electrolyte interphase (SEI). Instead, this true loss in capacity means some active particles became fully and irreversibly deactivated or electrochemically isolated. For the remaining functional particles, host concentration C_{a0}^H is unchanged and cycling can still occur across the full range of $0 < s < 1$ and, importantly, corresponding open circuit potential. Q_a^H naturally describes the diminished electrode areal capacity, by virtue of ϵ_{a0} , which in turn depends on χ_a .

Electrode running capacity per mass of active material, commonly used to describe charge or discharge experiments, is

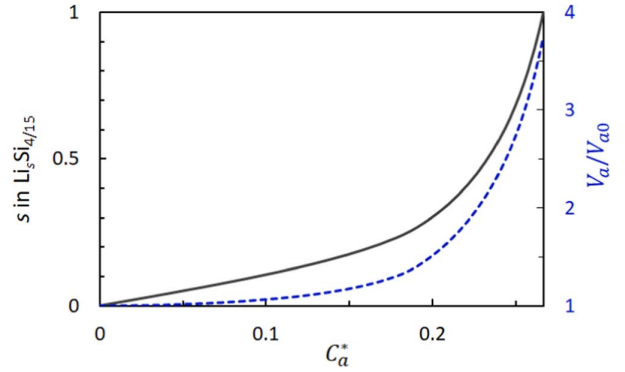


Figure 7. State of lithiation and active material volume for Si as functions of dimensionless Li concentration, $0 < C_a^* < \frac{4}{15}$.

computed from

$$q_a = s_{\text{avg}} \chi_a \mathcal{F} / \mathcal{M}_a \quad [60]$$

where $\mathcal{F} / \mathcal{M}_a = 3578$ mAh/g for Si_{4/15}. Equation 60 can be used to determine experimentally a global χ_a value because s_{avg} is controlled and known by means of the OCP in a half cell.

Hysteresis in open circuit potential.—We expect the open circuit potential (OCP or U) of Si to depend on SoL, temperature, and stress state. There is a significant OCP gap between lithiation and delithiation of Si electrodes according to multiple studies.^{20,70–72} This path dependence could be attributed to sluggish kinetics and diffusion of Si electrodes or to true (thermodynamic) hysteresis in Si, such as caused by chemical and plastic strains inside the particles that lead to residual stresses, or by metastable phase transformation behavior. If not a true hysteresis, then cycling the cell slowly (i.e. near equilibrium) would eliminate the kinetic and diffusional effects; however, a significant difference between Si lithiation and delithiation potential curves has still been observed even at very low C-rates.²⁰ This is illustrated in Fig. 8b.

Ignoring the observed hysteresis loop by averaging the two OCP curves could lead to substantial model errors. We further wish for a numerically stable method that allows for an arbitrary charge/discharge profile. Therefore the approach is to switch between these two curves in a continuous fashion. What follows is our method to do this.

We know that the standard-state OCP for an arbitrary charging history is bounded by lithiation (U_+^*) and delithiation (U_-^*) curves; thus, we define a dynamic variable $0 \leq \zeta \leq 1$ that locates the potential relative to the two curves, which in turn are functions of s evaluated on the particle surface:

$$U^* = \zeta U_+^* + (1 - \zeta) U_-^* \quad [61]$$

Inspired by Plett,⁷³ we define a PDE to dynamically switch between the curves:

$$\frac{\partial \zeta}{\partial s} = \beta \operatorname{sgn}(\dot{s}) [H(\dot{s}) - \zeta] \quad [62]$$

in which $H(\dot{s}) = [1 + \operatorname{sgn}(\dot{s})]/2$ is the Heaviside step function and \dot{s} is the time derivative of s at $r^* = 1$ and x^* . β is a dimensionless constant that controls how fast an asymptotical value ($\zeta = 0, 1$) is reached. Inserting $\operatorname{sgn}(\dot{s}) = |\dot{s}|/\dot{s}$ and using the chain rule, Eq. 62 can be recast in the time domain:

$$\frac{\partial \zeta}{\partial t} \Big|_{x^*} = \beta |\dot{s}| [H(\dot{s}) - \zeta] \quad [63]$$

Figure 8a illustrates the effect of different values of β . Figure 8b shows that with $\beta = 30$ the OCP can rapidly transition between the

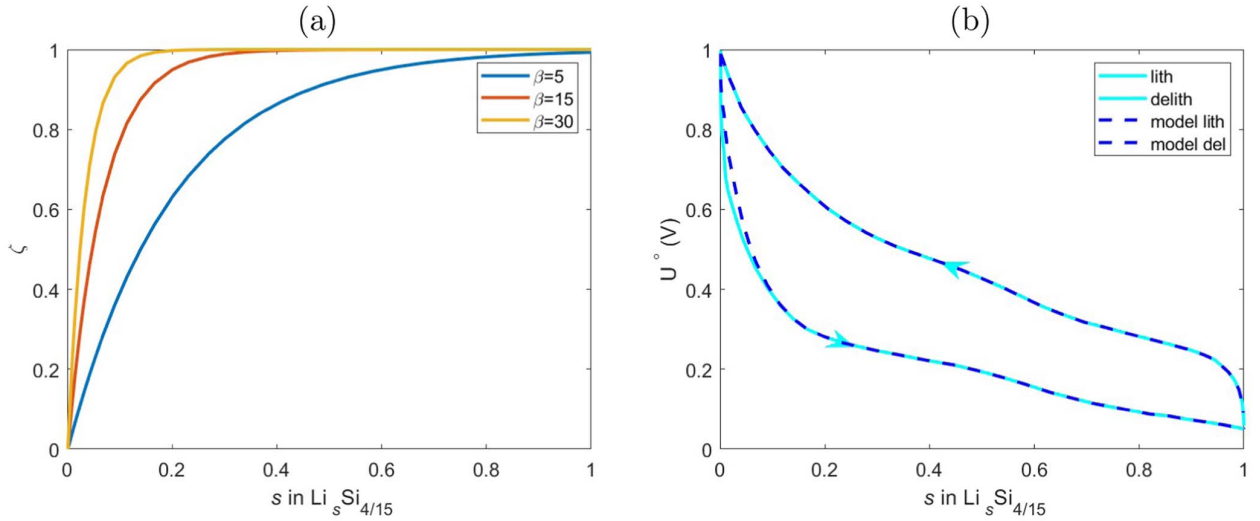


Figure 8. (a) Switching function ζ during a lithiation cycle for $\beta = 5, 15, 30$. (b) Simulation of Si OCP showing that $\beta = 30$ can provide a realistically rapid transition between lithiation (lower) and delithiation (upper) curves,²¹ also indicated by arrows, when the current direction is changed at $s = 0, 1$.

lithiation and delithiation curves as expected when the current changes direction.

Effect of stress on open circuit potential.—The OCP hysteresis model above effectively treats any particle residual stresses due to lithiation and delithiation, but does not necessarily account for externally imposed surface normal stress or equivalently pressure. In case this is significant, its effect on OCP is considered here. For perspectives related to the topic of particle stresses and OCP, please see.⁷⁴

The overall chemical reaction for the half cell is given in Eq. 1. Therefore the half-cell OCP is

$$U = \frac{1}{\mathcal{F}}(\mu_{\text{Li}} + \mu_{\text{Si}_{4/15}} - \mu_{\text{LiSi}_{4/15}}) \quad [64]$$

where μ_i is species i chemical potential. U can be expanded in terms of homogenized surface pressure P of the respective active materials:

$$U = U^\circ + \frac{1}{\mathcal{F}}[(P_{\text{Li}} - P^\circ) \bar{V}_{\text{Li}} + (P_a - P^\circ)(\bar{V}_{\text{Si}_{4/15}} - \bar{V}_{\text{LiSi}_{4/15}})] + O(P^2) \quad [65]$$

where U° is the OCP function when the active surfaces are maintained at standard state pressure $P^\circ = 1$ bar. $\bar{V}_i = \partial\mu_i/\partial P$ is species partial molar volume. The second-order term $O(P^2)$ in Eq. 65 is eliminated if volume change due to elastic compression of the active material is relatively small, an assumption already made in our particle model.

Several principles are used to simplify and evaluate Eq. 65. The Li counter electrode is a pure solid, so partial molar volume becomes the molar volume of Li metal: $\bar{V}_{\text{Li}} = V_{\text{Li}}$. The remaining two species form a solid solution in the Si active material, obeying the summability relation $V_a = s\bar{V}_{\text{LiSi}_{4/15}} + (1-s)\bar{V}_{\text{Si}_{4/15}}$ where V_a was previously defined and s takes the role of mole fraction. Therefore $\bar{V}_{\text{LiSi}_{4/15}} - \bar{V}_{\text{Si}_{4/15}} = \partial V_a/\partial s$. Putting all this together leads to

$$U = U^\circ + \frac{1}{\mathcal{F}} \left[(P_{\text{Li}} - P^\circ) V_{\text{Li}} - (P_a - P^\circ) \frac{\partial V_a}{\partial s} \right] \quad [66]$$

And we can further state from Eq. 2 that $\partial V_a/\partial s = V_{a0} \min\left(\frac{539}{48}s, \frac{77}{24}\right)$ where s is evaluated on the particle surface.

The homogenized surface pressures on the active materials in Eq. 66 are each derived from the negative average of the principal electrode stresses:

$$P_a - P^\circ = -\frac{1}{3}(\sigma_x + 2\sigma_y)(E_a/E)^m \quad [67]$$

The term $(E_a/E)^m$ corrects for the portion of the load on the electrode that is exerted on just the active material, as opposed to the inert material, consistent with Eq. 24. The stresses can be evaluated in terms of strains by means of Eq. 4. Equation 67 assumes that the background medium (i.e. liquid electrolyte) is at the standard pressure P° . If this were not the case, an adjustment could be made, though only a very large liquid pressure would contribute noticeably to the OCP.

To experimentally determine OCP, one commonly performs the low-rate lithiation and delithiation of the working electrode under mildly compressive normal stress (such as in a coin cell) and subsequently assumes the measured half-cell potential to be U° . However, Eq. 67 shows that even when the stack pressure ($-\sigma_x$) is small, $P_a - P^\circ$ can be quite large in a silicon-based electrode due to tangential stress σ_y . Equation 66 then shows that measured U can decrease significantly from U° and the two should not be treated as equal. Therefore, U_+° and U_-° curves reported in the literature should be corrected before use in the model, so that this displacement of U caused by naturally occurring tangential stress is not double-counted.

Reactions, potentials, and currents.—As in conventional P2D models, potentials and currents are described for the homogenized electrolyte and solid phases, respectively denoted by subscripts e and s . The solid phase comprises both the active and inert components. Faradaic reactions take place at the interface between the electrolyte and solid phases.

The distributed Si reaction and Li foil reaction each are described with symmetric Butler-Volmer kinetics:

$$\mathcal{F}j_a^{\text{rxn}} = i_0 [e^{a\mathcal{F}\eta/RT} - e^{-(a-1)\mathcal{F}\eta/RT}] \quad [68]$$

Variables take their usual electrochemical meaning² and $\alpha = 0.5$ by default. The reaction overpotential is

$$\eta = \Phi_s - \Phi_e - U \quad [69]$$

For the foil boundary at $x^* = 2$ we constrain $\Phi_s = U = 0$ and let the exchange current density for $j_{\text{foil}}^{\text{rxn}}$ be

$$i_0 = i_0^{\text{ref}} \left(\frac{C_e}{C_{e0}} \right)^\alpha \quad [70]$$

where C_{e0} is both the initial and reference concentration. For the reaction distributed across the electrode, we instead let

$$\begin{aligned} i_0 &= i_0^{\text{ref}} \left(\frac{C_e}{C_{e0}} \right)^\alpha \left(\frac{C_a^H - C_a}{C_{a0}^H} \right)^\alpha \left(\frac{C_a}{C_{a0}^H} \right)^{1-\alpha} \\ &= i_0^{\text{ref}} \left(\frac{C_e}{C_{e0}} \right)^\alpha (s^{-1} - 1)^\alpha C_a^* \end{aligned} \quad [71]$$

where C_{a0}^H in the denominator serves as a reference concentration and C_a , C_a^* , and s are evaluated on the particle surface, $r^* = 1$. The second line in Eq. 71 is derived from $C_a^* = C_a/C_{a0}^H$ and Eq. 55. Likewise, s is computed from Eq. 56 with this C_a^* as the argument. The respective values of i_0^{ref} for Eqs. 70 and 71 are given in Table I.

The cell potential is determined by the potential difference between the current collectors, where the Li foil potential is set to zero:

$$\mathcal{E}_{\text{cell}} = 0 - \Phi_{s,x^*=0} \quad [72]$$

As expected, in the limit of zero current and concentration gradient, $\mathcal{E}_{\text{cell}} \rightarrow U$.

The remaining parts of the model follow conventional P2D equations² albeit with localized strain and porosity dependence. To determine the solid and electrolyte potentials, two charge conservation PDEs must be solved on x^* :

$$-\frac{\partial I_s}{\partial x^*} = \frac{\partial I_e}{\partial x^*} = \mathcal{F} a_a j_a^{\text{rxn}} L_\theta \quad [73]$$

where the superficial current densities for solid and electrolyte are respectively

$$\begin{aligned} I_s &= -\frac{\kappa_s}{L_\theta} \frac{\partial \Phi_s}{\partial x^*} \\ I_e &= -\frac{\kappa_e}{L_\theta} \left[\frac{\partial \Phi_e}{\partial x^*} - \frac{2RT(1-t_+^0)}{\mathcal{F} C_e} \left(1 + \frac{\partial \ln f_{\pm}}{\partial \ln C_e} \right) \frac{\partial C_e}{\partial x^*} \right] \end{aligned} \quad [74]$$

Additional boundary conditions are

$$\begin{aligned} I_s &= -I_{\text{app}} & \text{at } x^* &= 0 \\ I_s &= 0 & \text{at } x^* &= 1 \\ I_e &= 0 & \text{at } x^* &= 0 \\ I_e &= -\mathcal{F} j_{\text{foil}}^{\text{rxn}} & \text{at } x^* &= 2 \end{aligned} \quad [75]$$

with Φ_e and I_e being continuous across the adjacent layers at $x^* = 1$.

Effective electrolyte conductivity in the electrode and separator layers has a dependence on porosity that mirrors Eq. 37.^{65,66}

$$\kappa_e = \kappa_e^{\text{int}} \gamma^{-1} \epsilon^{1.5} \quad [76]$$

where κ_e^{int} is intrinsic conductivity of the electrolyte. MacMullin Number, used as a dimensionless ionic resistivity, is defined as $N_M = D_e^{\text{int}}/D_e = \kappa_e^{\text{int}}/\kappa_e$. Solid-phase electronic conductivity κ_s has a power-law porosity dependence that mirrors Eq. 23:⁷⁵

$$\kappa_s = \kappa_s^{\text{int}} (1 - \epsilon)^{1/m} \quad [77]$$

However, it should be noted that κ_s^{int} is large enough here (Table I) that the porosity dependence has a negligible effect on outcomes.

Results and Discussion

Although the model development in the previous Section is lengthy, implementing the equations in COMSOL Multiphysics was

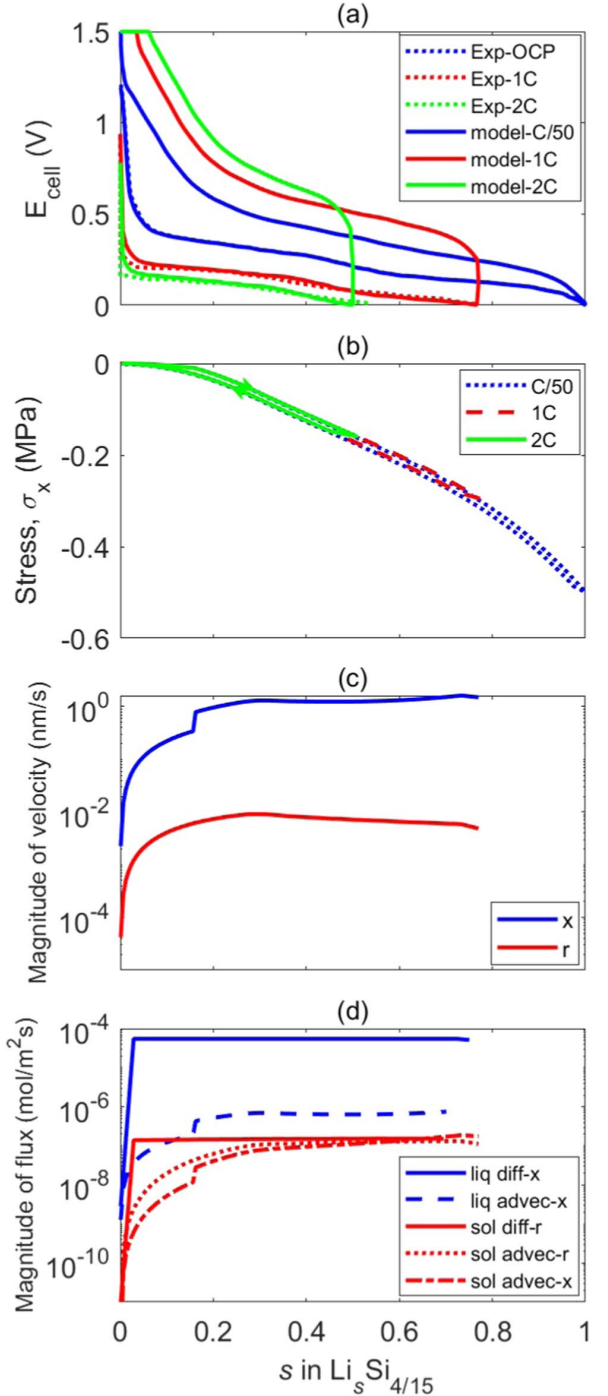


Figure 9. Baseline model results vs. SoL for (a) cell potential at three C-rates compared to experimental results,⁶⁷ (b) normal stress at three C-rates, (c) Li velocity magnitude in x and r directions for 1C lithiation, and (d) Li flux magnitude for diffusion and advection for 1C lithiation. The soft casing is used throughout.

relatively straightforward as an extension of a standard P2D model.² In this Section simulation results of a representative Si electrode half-cell are presented.

Parameter selection.—The mechanical and electrochemical parameters used in this model are provided in Table I for the silicon

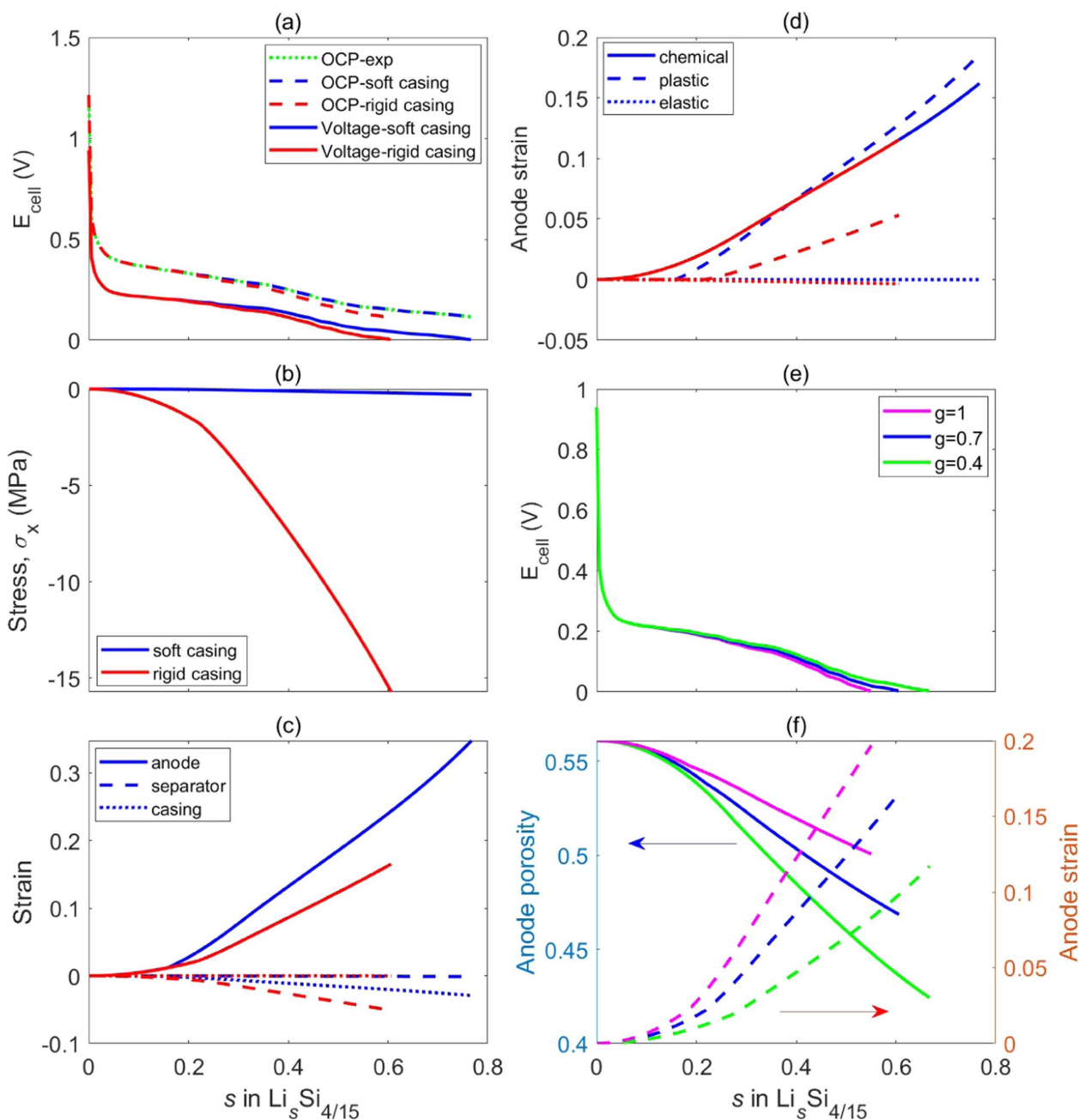


Figure 10. Baseline soft (blue curves) and rigid (red curves) casing designs are compared for 1C lithiation for (a) cell voltage and OCP compared to the experimental OCP; (b) normal stress; (c) total strain of the anode, separator, and casing layers; and (d) decomposition of anode strain into chemical, plastic, and elastic components. Rigid casing model sensitivity to swelling coefficient g during 1C lithiation for (e) cell voltage and (f) anode porosity and strain. Anode strains and porosity throughout are reported at $x^* = 0.99$, adjacent to the separator.

anode, separator, Li foil, current collectors, and casing. The electrode thickness and volume fractions come from experiments by Pan et al. for an electrode with composition 6:2:2 by mass of Si:C:PAA and functional capacity $q_a^{\max} = 1950 \text{ mAh/g Si}$,⁶⁷ leading to $\chi_a = 0.545$. This electrode has effective areal capacity $Q_a^H = 0.87 \text{ mAh/cm}^2$, upon which the C-rates are based. The OCP curves for Si (de)lithiation are obtained from,²¹ as are several other electrochemical parameters. Volumetric and mechanical properties are consistent with those used to generate Figs. 1–5. Remaining parameters such as electrolyte properties (often a function of

concentration and temperature) are available in our prior publications.^{2,3} The cell temperature is maintained at 25 °C.

The intention here is to focus on the silicon electrode, hence the use of a half-cell. However, even a Li metal counter electrode exhibits substantial volume changes upon stripping and deposition, compared to a traditional porous cathode. Furthermore, Li metal is highly malleable, with yield strength below 1 MPa. Therefore in order to mechanically imitate a more traditional cell, we turned off the chemical strain of the Li foil layer and eliminated its plasticity, while maintaining its elastic response to stress and its

electrochemical role as a source and sink for Li^+ . Eliminating the chemical strain effectively removes the term containing V_{Li} in Eq. 66.

Two variants are used for the casing layer. A soft or compliant casing with $E = 0.01$ GPa imitates a pouch or coin cell where cell strain is readily allowed and σ_x is negligible. A rigid or stiff casing with $E = 100$ GPa imitates a spirally wound 18650 cell in which essentially no cell volume change is allowed, such that strain in the Si electrode must be accommodated almost entirely by strain in the separator.

Baseline cell response.—Figure 9 shows results from baseline soft-casing simulations, where the model completes a lithiation-delithiation cycle of the Si electrode at various C-rates. In panel a, lithiation voltage-capacity curves are compared against experimental lithiation data from coin cells.⁶⁷ The OCP in reference⁶⁷ is assumed to be at C/50. Note that lithiation cycles are stopped when the voltage reaches 0, consistent with the practice of preventing lithium plating on the anode. The Si exchange current density i_0^{ref} and solid diffusivity D_a were adjusted to match the model to the experiment. The derived diffusivity is lower than that reported in Ref.67 and , but matches that in Ref.20. One source of difference may be the choice of representative Si particle radius in the model, which inherently couples with the diffusivity, and here is assumed to be 40 nm. In any case, the model satisfactorily fits the experimental lithiation curves.

To briefly examine the effect of particle size, the model was rerun with $R_{a0} = 80$ nm. While not shown in Fig. 9a, this resulted in modest changes. The OCP curve shifted downward by approximately 7 mV due to stress effects. Refitting the model to the experimental 1C and 2C lithiations yielded increased parameters $D_a = 10^{-17}$ m²/s and $i_0^{\text{ref}} = 0.034$ A/m². This 10-fold increase in diffusivity indicates that the baseline model is primarily diffusion limited.

Returning to the baseline model, Fig. 9b shows the generation of normal stress during a full cycle. As similarly observed in Fig. 4, there is a modest hysteresis between lithiation and delithiation originating from plastic strain in the electrode. The compliant casing accommodates most of the electrode swelling and the stack pressure reaches a maximum of 0.5 MPa at the end of lithiation for the lowest C-rate, which coincides with the highest achieved degree of lithiation. This degree of stress or pressure is consistent with coin-cell packaging, as intended.

Panel c shows how velocities u_x and u_r evolve during 1C lithiation, evaluated in the Si electrode next to the separator. The

velocity is much greater in the x direction, consistent with the greater length scale involved. Panel d similarly presents the magnitude of fluxes from diffusion and advection in both phases. Electrolyte diffusive flux magnitude is greater than advective. In the solid phase, advective flux magnitudes are initially smaller than radial diffusion, but by the end of lithiation are comparable in magnitude. Not shown in the plot is that the diffusive fluxes are consistently in the opposite direction from the corresponding advective fluxes, regardless of phase.

Effect of casing rigidity.—An important question for Si cells is the effect of packaging on cell performance, as represented here by casing Young's modulus. The baseline model with soft casing emulates coin and pouch cells in which the stack volume changes without generating significant normal stress. In contrast, a rigid casing layer with $10^4 \times$ higher modulus represents spirally wound cells inside a stainless steel can that does not permit significant stack expansion. Figure 10 compares results for the two casing designs during lithiation. Panel a illustrates how a rigid casing affects 1C cell voltage and corresponding anode utilization. OCP for the same simulations is also shown. The increased stack pressure from the rigid casing causes cell OCP to drop according to Eq. 66, thus causing the cutoff voltage to be reached at lower SoL. Therefore, constraining the volume can diminish electrode utilization.

Panel b shows how the normal stress, which is uniform across the cell sandwich and is the negative of stack pressure, increases in magnitude as lithiation proceeds. The maximum magnitude of 15 MPa for the rigid casing is substantial when compared to the soft casing (also compare this plot to the zoomed-in view in Fig. 9b).

Panel c demonstrates how strain is distributed among each layer in the cell sandwich, excluding lithium metal and current collectors. The effective stiffness of the porous separator lies between those of the anode and compliant casing; however, the separator is the softest of the three layers when the casing is rigid. Thus, in the latter scenario, the separator accommodates nearly all the Si electrode swelling, instead of the casing itself in the compliant casing scenario. A more detailed view of the anode strain is given in panel d. The chemical strain $k\theta_*$ follows the same path regardless of the casing type, although larger chemical strain eventually manifests in the (blue) soft casing scenario, due to increased electrode utilization. On the other hand, plastic deformation is more pronounced in the soft scenario and occurs earlier than in the rigid scenario. Finally, the generated stress magnitude and hence elastic strain is higher with the rigid scenario.

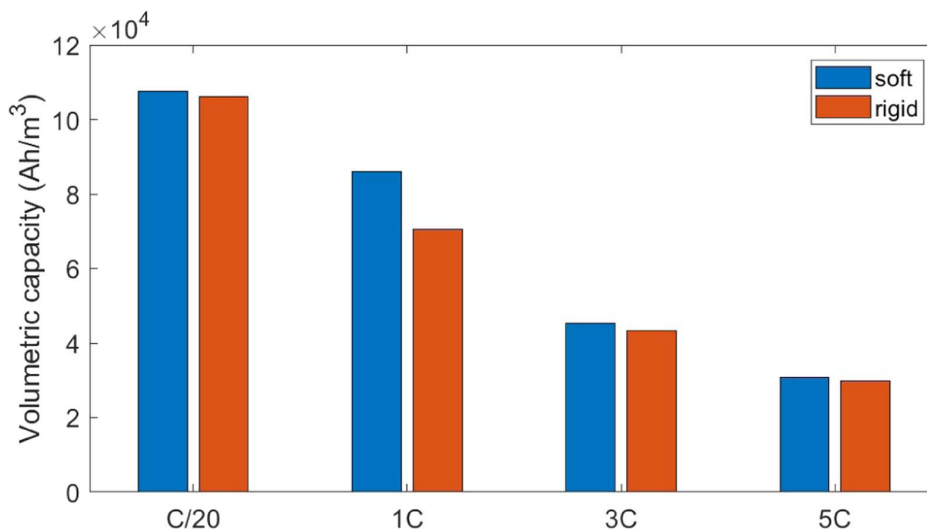


Figure 11. The volumetric capacity of the baseline compliant cell compared to the cell with rigid casing at various C-rates.

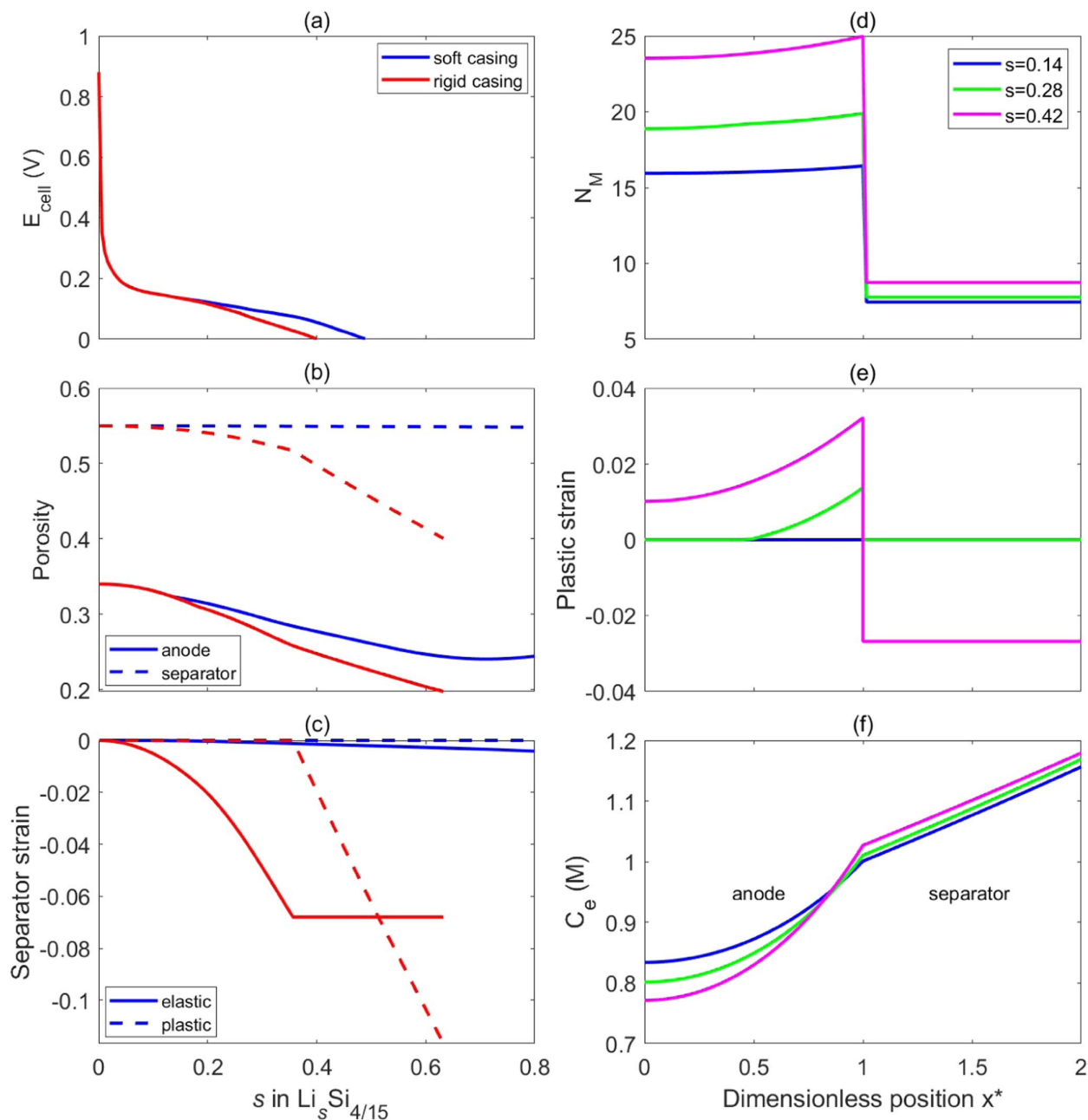


Figure 12. Cell performance at $5 \times$ loading and 1C lithiation under soft (blue curves) and rigid (red curves) casing scenarios for (a) cell voltage, (b) anode (at the anode/separator interface) and separator porosities, and (c) separator strains. Properties for the rigid scenario at 3 states of lithiation as a function of dimensionless position for (d) MacMullin number, (e) plastic strain, and (f) electrolyte concentration.

The baseline model was matched to electrochemical experiments in Fig. 9a for a cell with a soft casing and, unfortunately, no associated strain measurements. Hence, we cannot determine what g value is most accurate for that cell. Due to this uncertainty, Fig. 10e–f explores how cell behavior is influenced by a representative range of Si electrode swelling. The baseline $g = 0.7$ value is tested against lower and higher g values at 1C lithiation. The rigid casing is selected for this sensitivity analysis as the soft casing generates a less noticeable response. Panel e depicts anode utilization by the intercept at zero cell voltage; utilization is higher with a lower g value. A lower g leads to reduced stress because, as shown in panel f, a lower g leads to a greater reduction in porosity and hence greater electrode volume

change upon lithiation. Relatedly, though not shown, performance across different g values also depends on the C-rate due to variations in the degree of lithiation.

An alternative way to assess electrode utilization is through the volumetric capacity of the cell, $Q_a^{\max}/L_{\text{stack}}$, a property which incorporates the aggregate thickness of the cell stack at the end of lithiation while excluding the casing layer. Figure 11 shows volumetric capacity as a function of C-rate. The soft casing yields a higher volumetric capacity at all C-rates due to having higher SoL at the voltage cutoff point, in turn primarily due to less stack pressure and hence a larger value of OCP. This is in spite of the soft casing having somewhat larger stack thickness than the rigid casing,

which would tend to lower volumetric capacity. Note that the difference between casing designs is more substantial at 1C rate. This can be explained by the relative shallowness of the OCP curve for $0.6 < s < 0.8$, the range where 1C lithiation terminates (see Fig. 10a), leading to more sensitivity to casing-induced stack pressure.

Effect of active material loading.—Thus far, results have been presented for an electrode with initial $8.5 \mu\text{m}$ thickness and 56% porosity, resulting in a loading of 0.87 mAh/cm^2 . To gain a better understanding of cell performance with both soft and rigid casings, we contrast the baseline results with those for a high-energy cell with Si loading increased five-fold. The new simulated electrode design features an initial $28 \mu\text{m}$ thickness and 34% porosity, with commensurate $30 \mu\text{m}$ thickness for the Li foil. All other parameters remain at Table I values. Figures 12a–12c illustrates $5 \times$ loaded cell properties during 1C lithiation for the soft (blue curves) and rigid (red curves) casing scenarios. Panel a shows that increased loading accentuates the difference in the electrode utilization, compared to baseline loading (Fig. 10a). Panel b shows that the rigid casing causes porosity to be lower for both anode and separator and to a degree that can potentially limit ionic transport at the end of lithiation. Panel c reveals the elastic and plastic strain components within the separator. With the soft casing, plastic deformation remains at zero, whereas the rigid casing results in considerable separator plastic strain, which essentially means that the separator is being semi-permanently crushed. It should be noted that the behavior simulated in panels b and c, unlike panel a, includes constant-voltage lithiation after the 1C constant-current lithiation to 0 V.

Figure 12d–f shows property spatial variations within the anode and separator layers for three states of lithiation and a rigid casing. Dimensionless position $x^* < 1$ indicates the anode region and $x^* > 1$ indicates the separator region. In panel d, MacMullin Number, which is a dimensionless ionic resistance in the pores, increases as lithiation progresses due to the reduction in porosity. N_M takes its highest value in the anode next to the separator because of the greater lithiation at that position. As expected, N_M is uniform across the separator but increases with time as the separator is compressed.

Panel e shows that plastic yielding initiates at the separator and propagates into the anode, in response to the moving lithiation reaction front. Meanwhile, plastic strain is zero or compressive in the separator, consistent with panel c. Both ionic resistance and plastic strain remain uniform across the separator, as there is no chemical strain acting on it. Interestingly and non-intuitively, plastic strain in the anode is elongational, which is opposite in sign to the elastic strain. This retrograde behavior is caused by the presence of chemical strain and the tangential zero-strain condition ($\theta_y = 0$). It is also observed in Fig. 10d.

Lastly, panel f shows electrolyte concentration across the two layers. The polarization occurs largely as expected, with depletion of the electrolyte in the anode over the course of lithiation.

Conclusions

This work presents an internally consistent and numerically efficient P2D model for Si anodes in which large and local volume changes impact electrode microstructure, cell geometry, and consequently Li transport pathways, reactions, and overall cell performance. The developed mechanical model requires minimal experimental parameters considering the substantial mechanical behavior now included.

As illustrated in Figs. 4 and 12, the model predicts non-monotonic variations in electrode porosity during lithiation, influenced by subtle mechanical effects. Plastic yielding in the electrode film is pervasive, making it an essential aspect of the model to accurately capture stress and strain effects. Similarly, the significant hysteresis and stress dependence in the OCP of Si are appropriately incorporated.

In the course of model parameterization and validation, a thorough review of prior experimental studies on Si revealed several uncertainties and anomalies, as depicted in Figs. 1–3. Having a

detailed physical model allows for better evaluation of experimental reliability. At the same time, comparing to multiple experiments keeps the modeler honest. Feedback in both directions is particularly needed for Si-based electrodes that exhibit complex behaviors.

The model teaches that selecting the appropriate mechanical compliance for the packaging is crucial when designing Si-based cells. A compliant casing allows for greater cell thickness increase and reduced stack pressure, which can enhance the utilization of Si electrodes due to a more positive OCP and reduced ionic resistance. Higher Si loading accentuates this effect of casing design on electrode utilization. However, we note that the current model has not been made to account for degradation incurred at both particle and electrode levels by extensive Si particle swelling.⁷⁶ It may be that high stack pressure imposed by a rigid casing could be beneficial to long-term cell health even if not beneficial to single-cycle performance.

Acknowledgments

The authors gratefully acknowledge EnPower Inc., for partially funding this work.

ORCID

Amir-Sina Hamed  <https://orcid.org/0000-0002-1363-7823>
Dean R. Wheeler  <https://orcid.org/0000-0001-5017-3194>

References

1. M. Doyle, T. F. Fuller, and J. Newman, "Modeling of galvanostatic charge and discharge of the lithium/polymer/insertion cell." *J. Electrochem. Soc.*, **140**, 1526 (1993).
2. A.-S. Hamed, F. Pouraghajan, F. Sun, M. Nikpour, and D. R. Wheeler, "Interplay of electrode heterogeneity and lithium plating." *J. Electrochem. Soc.*, **169**, 020551 (2022).
3. A.-S. Hamed, A. Yao, R. Martin, R. Roig, M. R. Valadez, D. Pile, A. Shellikeri, B. Liu, and D. R. Wheeler, "Multi-layer anodes for high-current applications." *Electrochimica Acta*, **439**, 141649 (2023).
4. M. N. Obrovac, L. Christensen, D. B. Le, and J. R. Dahn, "Alloy design for lithium-ion battery anodes." *J. Electrochem. Soc.*, **154**, A849 (2007).
5. A. J. Louli, J. Li, S. Trussler, C. R. Fell, and J. R. Dahn, "Volume, pressure and thickness evolution of li-ion pouch cells with silicon-composite negative electrodes." *J. Electrochem. Soc.*, **164** (2017).
6. L. Beaulieu, T. Hatchard, A. Bonakdarpour, M. Fleischauer, and J. Dahn, "Reaction of Li with alloy thin films studied by in situ afm." *J. Electrochem. Soc.*, **150**, A1457 (2003).
7. J. Hou, S. Qu, M. Yang, and J. Zhang, "Materials and electrode engineering of high capacity anodes in lithium ion batteries." *Journal of Power Sources*, **450**, 227697 (2020).
8. W.-J. Zhang, "A review of the electrochemical performance of alloy anodes for lithium-ion batteries." *Journal of Power Sources*, **196**, 13 (2011).
9. A. Mukanova, A. Jetybayeva, S.-T. Myung, S.-S. Kim, and Z. Bakenov, "A mini-review on the development of Si-based thin film anodes for li-ion batteries." *Materials Today Energy*, **9**, 49 (2018).
10. H. Dasari and E. Eisenbraun, "Predicting capacity fade in silicon anode-based Li-ion batteries." *Energies*, **14**, 1448 (2021).
11. A. Durdal, S. Friedrich, L. Hsken, and A. Jossen, "Modeling silicon-dominant anodes: Parametrization, discussion, and validation of a newman-type model." *Batteries*, **9**, 558 (2023).
12. C. Zhang, S. Santhanagopalan, M. A. Sprague, and A. A. Pesarani, "A representative-sandwich model for simultaneously coupled mechanical-electrical-thermal simulation of a lithium-ion cell under quasi-static indentation tests." *Journal of Power Sources*, **298**, 309 (2015).
13. B. Rieger, S. V. Erhard, K. Rumpf, and A. Jossen, "A new method to model the thickness change of a commercial pouch cell during discharge." *J. Electrochem. Soc.*, **163**, A1566 (2016).
14. M. Wang, X. Xiao, and X. Huang, "A multiphysics microstructure-resolved model for silicon anode lithium-ion batteries." *Journal of Power Sources*, **348**, 66 (2017).
15. W. A. Appiah, J. Park, S. Byun, I. Cho, A. Mozer, M.-H. Ryou, and Y. M. Lee, "A coupled chemo-mechanical model to study the effects of adhesive strength on the electrochemical performance of silicon electrodes for advanced lithium ion batteries." *Journal of Power Sources*, **407**, 153 (2018).
16. B. Liu, Y. Jia, J. Li, H. Jiang, S. Yin, and J. Xu, "Multiphysics coupled computational model for commercialized Si/graphite composite anode." *Journal of Power Sources*, **450**, 227667 (2020).
17. Y. Chen, L. Yang, F. Guo, D. Liu, H. Wang, J. Lu, J. Zheng, X. Yu, and H. Li, "Mechanical-electrochemical modeling of silicon-graphite composite anode for lithium-ion batteries." *Journal of Power Sources*, **527**, 231178 (2022).
18. S. R. Shah, L. S. de Vasconcelos, and K. Zhao, "Computational modeling of electrochemomechanics of high-capacity composite electrodes in Li-ion batteries." *Journal of Applied Mechanics*, **89**, 081005 (2022).

19. X. Gao, W. Lu, and J. Xu, "Modeling framework for multiphysics-multiscale behavior of sic composite anode." *Journal of Power Sources*, **449**, 227501 (2020).
20. R. Chandrasekaran, A. Magasinski, G. Yushin, and T. F. Fuller, "Analysis of lithium insertion/deinsertion in a silicon electrode particle at room temperature." *J. Electrochem. Soc.*, **157**, A1139 (2010).
21. R. Chandrasekaran and T. F. Fuller, "Analysis of the lithium-ion insertion silicon composite electrode/separators/lithium foil cell." *J. Electrochem. Soc.*, **158**, A859 (2011).
22. S. Srivastav, C. Xu, K. Edström, T. Gustafsson, and D. Brandell, "Modelling the morphological background to capacity fade in Si-based lithium-ion batteries." *Electrochimica Acta*, **258**, 755 (2017).
23. S. Dhillon, G. Hernández, N. P. Wagner, A. M. Svensson, and D. Brandell, "Modelling capacity fade in silicon-graphite composite electrodes for lithium-ion batteries." *Electrochimica Acta*, **377**, 138067 (2021).
24. P. M. Gomadam and J. W. Weidner, "Modeling volume changes in porous electrodes." *J. Electrochem. Soc.*, **153**, A179 (2005).
25. T. R. Garrick, K. Higa, S.-L. Wu, Y. Dai, X. Huang, V. Srinivasan, and J. W. Weidner, "Modeling battery performance due to intercalation driven volume change in porous electrodes." *J. Electrochem. Soc.*, **164**, E3592 (2017).
26. T. R. Garrick, X. Huang, V. Srinivasan, and J. W. Weidner, "Modeling volume change in dual insertion electrodes." *J. Electrochem. Soc.*, **164**, E3552 (2017).
27. D. J. Pereira, J. W. Weidner, and T. R. Garrick, "The effect of volume change on the accessible capacities of porous silicon-graphite composite anodes." *J. Electrochem. Soc.*, **166**, A1251 (2019).
28. D. J. Pereira, M. A. Fernandez, K. C. Streng, X. X. Hou, X. Gao, J. W. Weidner, and T. R. Garrick, "Accounting for non-ideal, lithiation-based active material volume change in mechano-electrochemical pouch cell simulation." *J. Electrochem. Soc.*, **167**, 080515 (2020).
29. D. J. Pereira, A. M. Aleman, J. W. Weidner, and T. R. Garrick, "A mechano-electrochemical battery model that accounts for preferential lithiation inside blended silicon graphite (Si/C) anodes." *J. Electrochem. Soc.*, **169**, 020577 (2022).
30. F. A. L. Dullien, *Porous Media: Fluid Transport and Pore Structure* (Academic) 2nd ed. (1992).
31. M. P. Bonkile, Y. Jiang, N. Kirkaldy, V. Sulzer, R. Timms, H. Wang, G. Offer, and B. Wu, "Coupled electrochemical-thermal-mechanical stress modelling in composite silicon/graphite lithium-ion battery electrodes." *Journal of Energy Storage*, **73**, 108609 (2023).
32. W. Ai, L. Kraft, J. Sturm, A. Jossen, and B. Wu, "Electrochemical thermal-mechanical modelling of stress inhomogeneity in lithium-ion pouch cells." *J. Electrochem. Soc.*, **167**, 013512 (2020).
33. S. Arisetty and N. Jimenez, "and K Raghunathan. Modeling reversible expansion of porous electrodes in Si/NMC cells within the framework of multi-species, multi-reaction theory." *J. Electrochem. Soc.*, **169**, 110522 (2022).
34. Alexander Mendelson, *Plasticity: Theory and Application* (Macmillan, New York) Macmillan series in applied mechanics, (1968).
35. M.-T. F. Rodrigues et al., "Cell-format-dependent mechanical damage in silicon anodes." *ACS Applied Energy Materials*, **6**, 9243 (2023).
36. S. Cangaz, O. Lohrberg, T. Abendroth, C. Heubner, F. Schmidt, H. Althues, S. Drfler, A. Michaelis, and S. Kaskel, "Understanding substrate mechanics and chemo-mechanical behavior of columnar silicon films to enable deformation free anodes for high-energy Li-ion batteries." *Advanced Materials Interfaces*, **10**, 2202314 (2023).
37. Z. Guo and H. Yao, "Thickness gradient promotes the performance of si-based anode material for lithium-ion battery." *Materials & Design*, **195**, 108993 (2020).
38. D. Y. W. Yu, M. Zhao, and H. E. Hoster, "Suppressing vertical displacement of lithiated silicon particles in high volumetric capacity battery electrodes." *ChemElectroChem*, **2**, 1090 (2015).
39. D. C. Drucker and W. Prager, "Soil mechanics and plastic analysis or limit design." *Quarterly of Applied Mathematics*, **10**, 157 (1952).
40. B. Rieger, S. Schlueter, S. V. Erhard, and A. Jossen, "Strain propagation in lithium-ion batteries from the crystal structure to the electrode level." *J. Electrochem. Soc.*, **163**, A1595 (2016).
41. A. Y. R. Prado, M.-T. F. Rodrigues, S. E. Trask, L. Shaw, and D. P. Abraham, "Electrochemical dilatometry of Si-bearing electrodes: Dimensional changes and experiment design." *J. Electrochem. Soc.*, **167**, 160551 (2020).
42. D. Li, Y. Wang, J. Hu, B. Lu, D. Dang, J. Zhang, and Y.-T. Cheng, "Role of polymeric binders on mechanical behavior and cracking resistance of silicon composite electrodes during electrochemical cycling." *Journal of Power Sources*, **387**, 9 (2018).
43. R. Kumar, J. H. Woo, X. Xiao, and B. W. Sheldon, "Internal microstructural changes and stress evolution in silicon nanoparticle based composite electrodes." *J. Electrochem. Soc.*, **164**, A3750 (2017).
44. D.-H. Yoon, M. Marinaro, P. Axmann, and M. Wohlfahrt-Mehrens, "Study of the binder influence on expansion/contraction behavior of silicon alloy negative electrodes for lithium-ion batteries." *J. Electrochem. Soc.*, **167**, 160537 (2020).
45. V. B. Shenoy, P. Johari, and Y. Qi, "Elastic softening of amorphous and crystalline lisi phases with increasing li concentration: A first-principles study." *Journal of Power Sources*, **195**, 6825 (2010).
46. V. A. Sethuraman, M. J. Chon, M. Shimshak, N. Van Winkle, and P. R. Guduru, "In situ measurement of biaxial modulus of si anode for li-ion batteries." *Electrochemistry Communications*, **12**, 1614 (2010).
47. B. Hertzberg, J. Benson, and G. Yushin, "Ex-situ depth-sensing indentation measurements of electrochemically produced Si-Li alloy films." *Electrochemistry Communications*, **13**, 818 (2011).
48. J. B. Ratchford, B. A. Crawford, J. Wolfenstine, J. L. Allen, and C. A. Lundgren, "Young's modulus of polycrystalline Li₁₂Si₇ using nanoindentation testing." *Journal of Power Sources*, **211**, 1 (2012).
49. S. T. Boles, C. V. Thompson, O. Kraft, and R. Mng, "In situ tensile and creep testing of lithiated silicon nanowires." *Applied Physics Letters*, **103**, 26390612 (2013).
50. M. Pharr, Z. Suo, and J. J. Vlassak, "Measurements of the fracture energy of lithiated silicon electrodes of Li-ion batteries." *Nano Letters*, **13**, 5570 (2013).
51. L. A. Berla, S. W. Lee, Y. Cui, and W. D. Nix, "Mechanical behavior of electrochemically lithiated silicon." *Journal of Power Sources*, **273**, 41 (2015).
52. H. Sitinamaluwa, J. Nerkar, M. Wang, S. Zhang, and C. Yan, "Deformation and failure mechanisms of electrochemically lithiated silicon thin films." *RSC advances*, **7**, 13487 (2017).
53. Y. Wang, D. Dang, D. Li, J. Hu, and Y.-T. Cheng, "Influence of polymeric binders on mechanical properties and microstructure evolution of silicon composite electrodes during electrochemical cycling." *Journal of Power Sources*, **425**, 170 (2019).
54. Y. Wang, Q. Zhang, D. Li, J. Hu, J. Xu, D. Dang, X. Xiao, and Y.-T. Cheng, "Mechanical property evolution of silicon composite electrodes studied by environmental nanoindentation." *Advanced Energy Materials*, **8**, 1702578 (2018).
55. H. Xie, W. Qiu, H. Song, and J. Tian, "In situ measurement of the deformation and elastic modulus evolution in Si composite electrodes during electrochemical lithiation and delithiation." *J. Electrochem. Soc.*, **163**, A2685 (2016).
56. D. Li, Y. Wang, J. Hu, B. Lu, Y.-T. Cheng, and J. Zhang, "In situ measurement of mechanical property and stress evolution in a composite silicon electrode." *Journal of Power Sources*, **366**, 80 (2017).
57. A. P. Roberts and E. J. Garboczi, "Computation of the linear elastic properties of random porous materials with a wide variety of microstructure." *Proceedings of the Royal Society of London. Series A: Mathematical, Physical and Engineering Sciences*, **458**, 1033 (2002).
58. L. Gibson and M. Ashby, *Mechanics of Cellular Solids* (Pergamon Oxford, New York) (1988).
59. C. Deutsch, "Calculating Effective Absolute Permeability in Sandstone/Shale Sequences." *SPE Formation Evaluation*, **4**, 343 (1989).
60. H. Xie, Y. Kang, H. Song, and Q. Zhang, "Real-time measurements and experimental analysis of material softening and total stresses of Si-composite electrode." *Journal of Power Sources*, **424**, 100 (2019).
61. V. A. Sethuraman, A. Nguyen, M. J. Chon, S. P. Nadimpalli, H. Wang, D. P. Abraham, A. F. Bower, V. B. Shenoy, and P. R. Guduru, "Stress evolution in composite silicon electrodes during lithiation/delithiation." *J. Electrochem. Soc.*, **160**, A739 (2013).
62. J. Cannarella, X. Liu, C. Z. Leng, P. D. Sinko, G. Y. Gor, and C. B. Arnold, "Mechanical properties of a battery separator under compression and tension." *J. Electrochem. Soc.*, **161**, F3117 (2014).
63. G. Sikha, B. Popov, and R. White, "Effect of porosity on the capacity fade of a lithium-ion battery: Theory." *J. Electrochem. Soc.*, **151**, A1104 (2004).
64. R. B. Bird, W. Stewart, and E. Lightfoot, *Transport Phenomena* (Wiley, Hoboken, New Jersey) 2nd ed. (2007).
65. N. A. Zacharias, D. R. Nevers, C. Skelton, K. Knackstedt, D. E. Stephenson, and D. R. Wheeler, "Direct measurements of effective ionic transport in porous Li-ion electrodes." *J. Electrochem. Soc.*, **160**, A306 (2012).
66. I. V. Thorat, D. E. Stephenson, N. A. Zacharias, K. Zaghbi, J. N. Harb, and D. R. Wheeler, "Quantifying tortuosity in porous Li-ion battery materials." *Journal of Power Sources*, **188**, 592 (2009).
67. K. Pan, F. Zou, M. Canova, Y. Zhu, and J.-H. Kim, "Systematic electrochemical characterizations of si and sio anodes for high-capacity Li-ion batteries." *Journal of Power Sources*, **413**, 20 (2019).
68. F. Yang, "Interaction between diffusion and chemical stresses." *Materials Science and Engineering: A*, **409**, 153 (2005).
69. J. Li, N. Lotfi, R. G. Landers, and J. Park, "A single particle model for lithium-ion batteries with electrolyte and stress-enhanced diffusion physics." *J. Electrochem. Soc.*, **164**, A874 (2017).
70. T. D. Hatchard and J. R. Dahn, "In situ XRD and electrochemical study of the reaction of lithium with amorphous silicon." *J. Electrochem. Soc.*, **151**, A838 (2004).
71. M. Verbrugge, D. Baker, and X. Xiao, "Formulation for the treatment of multiple electrochemical reactions and associated speciation for the lithium-silicon electrode." *J. Electrochem. Soc.*, **163**, A262 (2015).
72. C.-H. Chen, F. Brosa Planella, K. O. Regan, D. Gastol, W. D. Widanage, and E. Kendrick, "Development of experimental techniques for parameterization of multi-scale lithium-ion battery models." *J. Electrochem. Soc.*, **167**, 080534 (2020).
73. G. Plett, *Battery management systems, Volume I: Battery modeling* (Artech House) (2015).
74. M. Kim, Z. Yang, and I. Bloom, "Review the lithiation/delithiation behavior of si-based electrodes: A connection between electrochemistry and mechanics." *J. Electrochem. Soc.*, **168**, 010523 (2021).
75. D. R. Nevers, S. W. Peterson, L. Robertson, C. Chubbuck, J. Flygare, K. Cole, and D. R. Wheeler, "The effect of carbon additives on the microstructure and conductivity of alkaline battery cathodes." *J. Electrochem. Soc.*, **161**, A1691 (2014).
76. A. Mukhopadhyay and B. W. Sheldon, "Deformation and stress in electrode materials for Li-ion batteries." *Progress in Materials Science*, **63**, 58 (2014).